# The intertidal zones of the South Atlantic Bight and their local and regional influence on astronomical tides

Peter Bacopoulos[a] and Scott C. Hagen[b]

**ABSTRACT:** Astronomical tides in the South Atlantic Bight are simulated with a fine-resolution (down to ~10 m), shallow-water equations, finite element model that fully represents the contiguous geometry of the system, including the: width- and depth-variable continental shelf; inlet-punctuated coastline; and riverine and intertidal character of the estuaries. Tidal levels are analyzed for the entirety of the South Atlantic Bight which produces highly detailed maps (resolution of 10–100 m) of tidal datums (MLW—mean low water, MHW—mean high water) throughout the estuarine rivers and intertidal zones. Model skill (performance) when evaluated over 142 gaging stations is $R^2$ = 92% for tidal datums (MLW and MHW) and less than 10% error for the full astronomical tide signal inside the estuaries, and within 0.01 m $s^{-1}$ error for $M_2$ shelf velocities. Tidal analysis reveals a sensitivity of the $M_2$-resonant shelf circulation in the South Atlantic Bight with respect to the tidal inlets, estuarine rivers and intertidal zones, primarily from the Florida/Georgia border to Winyah Bay (South Carolina). The inlets generate an 'openness' the South Atlantic Bight coastline, but more important are the geometric-dynamic influences of the estuarine rivers (the cause-effect being enhanced resonance due to extended effective shelf width) and intertidal zones (the cause-effect being tidal decay due to energy

[a] Corresponding author. Independent Subcontractor, 1431 Riverplace Blvd. 1201, Jacksonville, FL, 32207, USA. E-mail: busy_child29@hotmail.com. Phone: +1 850 570 0267. Fax: +1 850 570 0267.

[b] Professor, Louisiana State University, Department of Civil and Environmental Engineering / Center for Computation and Technology and Director, Center for Coastal Resiliency, 124C Sea Grant Hall, Baton Rouge, LA, 70803, USA.

dissipation). The riverine and intertidal features of the coastline subtly change the mode of tidal propagation over the continental shelf. Dynamically, the standing wave behavior (resonance) of astronomical tides in the South Atlantic Bight is a function of the shelf and coastline geometries. Modeling and assessment of coastal and shelf circulation should consider the domain as a continuum, including high-resolution definition of the coast's estuaries and intertidal zones.

***Keywords:*** South Atlantic Bight; Intertidal zone; Tidal datums; Continental shelf circulation; $M_2$ resonance; Tidal energy dissipation

## 1. Background and introduction

Atkinson et al. (1985) defined the South Atlantic Bight as the ocean and coastal domain extending from 27°N at West Palm Beach, Florida to 35°N at Cape Lookout, North Carolina (Figure 1). Distinguishing it from other U.S. coastal oceans, the continental shelf of the South Atlantic Bight varies from 40 to 140 km wide and the coastline (Florida, Georgia and the Carolinas) is perforated by numerous inlets (Shepard, 2015). There is a total of 64 inlets located along the South Atlantic Bight coastline, where Biscayne Bay, Florida is the southernmost inlet and Bogue Inlet, North Carolina is the northernmost (Table 1). This inlet catalogue for the South Atlantic Bight coastline excludes Beaufort Inlet, which services Pamlico Sound—a system of the Middle Atlantic Bight coastline. The Atlantic Intracoastal Waterway (AIW), a protected channel typically only 100 m wide (Parkman, 1983), connects the inlets and runs continuously along the entire length of the South Atlantic Bight coastline. Refer to Appendix A for a comprehensive geographic site assessment of the South Atlantic Bight. There are variable estuary types and shapes along the South Atlantic Bight coastline, ranging from convergent rivers (Seim et al.,

2006) to dissipative lagoons (Smith, 2001), while salt marshes populate the coastal boundary from northeast Florida to the South/North Carolina border, which extend 12 km inland at their greatest width in Georgia (Dame et al., 2000). The most recent inclusive (numerical modeling) coverage of coastal ocean circulation in the South Atlantic Bight was completed by Blanton et al. (2004) and Lynch et al. (2004); however, their domains did not consider the intertidal zones of the estuaries, which as we show in this paper constitute an important factor affecting tidal circulation in the South Atlantic Bight.

An objective of this paper is to examine a relatively smooth coast vs. bay/inlet vs. AIW vs. full intertidal zone influence on $M_2$ tidally driven circulation in the shelf waters of the South Atlantic Bight. The fully developed model includes a comprehensive definition of the estuaries and intertidal zones. As an outcome of the process, we develop a capability to simulate tides and compute tidal datums (HAT, MHHW, MHW, MSL, MLW, MLLW and LAT; refer to Table 2 for definitions and descriptions) at fine resolution for the full intertidal zone of the South Atlantic Bight. At the local scale, tidal datums (particularly MLW) have been shown to be highly spatially variable over the intertidal zones, especially compared with the 'smoothness' of the tidal-datum field over the main waterbody and channels of the estuary (e.g., see Hagen et al., 2012 for study of the Timucuan Preserve—St. Johns River). Regional maps of tidal datums for the entire South Atlantic Bight with local details of the estuaries and intertidal zones, which we generate herein, have direct relevance to physical oceanography (e.g., see Parker et al., 2003 for a review of geospatial and coastal oceanographic applications) as well as to estuarine ecology (e.g., see Alizad et al., 2016 for a study of *Spartina alterniflora*).

Tides in the South Atlantic Bight are dominated by the semi-diurnal frequency, primarily $M_2$, resulting from the co-oscillation with the western North Atlantic deep ocean tide (Redfield, 1958). South Atlantic Bight tides exhibit cross-shelf amplification (Battisti and Clarke, 1982), which is greatest where the shelf is widest off the Georgia coast (Figure 1). Cross-shelf amplification can be explained in terms of continental margin theory (Clarke and Battisti, 1981) with use of a scale factor:

$$\nu = \frac{a(\omega^2 - f^2)}{g\alpha} \tag{1}$$

where $a$ is the cross-shelf width, $\omega$ is the tidal frequency, $f$ is the Coriolis frequency (= $2\Omega\sin\varphi$), $\Omega$ is earth's rotation rate ($7.2921 \times 10^{-5}$ s$^{-1}$), $\varphi$ is the angle of latitude, $g$ is the acceleration due to gravity and $\alpha$ is the shelf bottom slope. With the shelf bottom slope approximated as the water depth $H$ at the shelf break divided by the cross-shelf width, i.e., $\alpha \sim H/a$, the scale factor becomes $\nu = a^2(\omega^2 - f^2)/gH$. Since $\nu$ increases like $a^2(\omega^2 - f^2)$, semi-diurnal tides are amplified on wide shelves (large $a$) in non-polar latitudes ($\omega_{\text{semi-diurnal}} > f_{\text{non-polar}}$). Using $\omega_{\text{semi-diurnal}} = 1.41(10^{-4})$ s$^{-1}$, $\omega_{\text{diurnal}} = 7.29(10^{-5})$ s$^{-1}$, and $f_{\text{SAB,30°N}} = 7.29(10^{-5})$ s$^{-1}$, semi-diurnal tides are amplified because the dominant $M_2$ frequency varies from the Coriolis frequency, i.e., ($\omega_{\text{semi-diurnal}}/f_{\text{SAB,30°N}} \sim 1.93) > 1$. On the other hand, the diurnal frequency is near equal to the Coriolis frequency, i.e., $\omega_{\text{diurnal}}/f_{\text{SAB,30°N}} \sim 1$, and hence, diurnal tides do not amplify.

In the context of continental margin theory, the variable shelf width of the South Atlantic Bight yields varying degrees of tidal amplification at the semi-diurnal frequency, viz. the quadratic relation of $\nu \propto a^2$. Blanton et al. (2004) showed $M_2$ tides in the South Atlantic Bight to be amplified as a result of the expansive shelf width as well as by the estuary-tidal inlet complex located along Georgia's coast; yet, the physical mechanism of the coupling between the shelf and inshore waters still has not been elucidated. Seim et al. (2006) demonstrated the tidal amplification in the Satilla River to follow the theory of strongly convergent estuaries (Friedrichs and Aubrey, 1994). Bacopoulos et al. (2012) found a ±20% sensitivity with respect to discharge in Clapboard Creek (St. Johns River) as influenced by bottom-friction characterization of the intertidal zones (Timucuan Preserve). Bruder et al. (2014) showed the tidal flats of the Ogeechee estuary to be the major controlling factor for the distortion of tidal hydrodynamics. The estuaries (e.g., shape) and intertidal zones clearly have local impacts on tidal hydrodynamics. But, given the regional scale of the estuaries and intertidal zones for the South Atlantic Bight coastline, is there a shelf-scale response to the coastline definition? It is paradoxical that a perforated coastline would amplify shelf circulation, while fundamental reasoning would suggest such a coastline to yield greater dissipation and thus dampening of shelf circulation. We hypothesize that: the inlets, estuaries and rivers of the South Atlantic Bight act to extend the effective shelf width which, in accordance with continental margin theory and the scale factor of Clarke and Battisti (1981), leads to a nonlinear (quadratic) increase in tidal dynamics, i.e., amplified shelf circulation; and the marshes and lagoons act as momentum dissipaters.

The paper is organized as follows. We present the modeling methods and requirements for tide simulation. The model is applied for assessment of astronomical tides throughout the intertidal zones (including model performance) and analysis of the physical mechanisms behind the estuarine and marsh influence on $M_2$-driven shelf circulation. Tidal mechanics, as generated by the high-resolution model of the South Atlantic Bight, permit for evaluation of shelf circulation in response to the coastal definition with inlets only, the inlets plus the AIW and the full intertidal zone. The implications of the analysis and results are discussed, after which the study is summarized and concluded. Two appendices contain a geographic site assessment of the South Atlantic Bight and a comprehensive model skill assessment.

## 2. Hydrodynamic modeling

### *2.1. Model description, assumptions and justification*

Tide simulations were carried out using the Advanced Circulation (ADCIRC) numerical code (Luettich et al., 1992) with high-resolution mesh description of the South Atlantic Bight, including all of its estuaries and intertidal zones. ADCIRC solves the shallow-water equations (hydrostatic pressure distribution) with finite-element discretization in space (linear Lagrange elements) and finite-difference discretization in time (three-level scheme) subject to forcing (boundary conditions) and source/sink (surface stress, bottom friction and lateral momentum dispersion) terms (Westerink et al., 2008). For the tide simulations presented herein, the barotropic, depth-integrated version of ADCIRC was applied in fully nonlinear mode, including advection, finite-amplitude effects and quadratic bottom stress (Parker, 1991), with wetting and drying of elements (Medeiros and Hagen, 2012). Tidal hydrodynamics in the South Atlantic Bight are primarily barotropic in mode (Lynch et al., 2004), whereby the use of depth-integrated flow (i.e., two-dimensional model) is considered valid given the longwave behavior of astronomic tides. The wetting and drying of the intertidal zones plays an important role in the tidal simulations conducted as part of this study.

### *2.2. Mesh development and domain definition*

The unstructured finite element mesh for the South Atlantic Bight was developed using localized truncation error analysis (Hagen et al., 2001) with complex derivatives (LTEA+CD; refer to Parrish and Hagen, 2009 for details). The target element size distribution generated by LTEA+CD prescribed relaxation of the mesh (i.e., larger element sizes) for the shelf and deeper waters and refinement of the mesh (i.e., smaller element sizes) for the shallow-water region, including more mesh nodes (density) near inlets and less mesh nodes (density) for the coastline in between adjacent inlets. Full details of the South Atlantic Bight mesh development are described in Bacopoulos et al. (2011); however, as a summary, approximately 90% of the mesh nodes are concentrated in the inshore regions, while the remaining ~10% of the mesh nodes describe the offshore regions.

The mesh telescopes from the western North Atlantic Ocean (bounded on the east by the 60-degree west meridian; see Hagen et al., 2006) into the South Atlantic Bight and through the inlets (64 total), AIW, estuaries, rivers, marshes and lagoons (Figure 1). The comprehensive mesh of the South Atlantic Bight describes the river-to-sea continuum from the upstream limit of tidal influence to the shelf break and deep ocean. Since the landward edge of the mesh extends to the limit of tidal influence, no-flow boundary conditions are applied along the landward boundary of the model. The model is forced by tide-elevation boundary conditions on the open-ocean boundary of the model. The mesh resolution ranges from approximately 10 to 1000 m (50–100 m in general) in the inshore regions (see Figure 2 for some examples: definition of the St. Johns River at the estuary scale; and representation of the tidal creek-salt marsh system of the Timucuan Preserve), while the mesh resolution ranges from 1 to 20 km in the offshore regions.

Mesh bathymetry is based on data sourced from the St. Johns River and South Florida Water Management Districts, U.S. Army Corps of Engineers, Office of Coast Survey and National Geophysical Data Center. Mesh topography is based on the U.S. Geological Survey National Elevation Dataset, i.e., bare-earth data with horizontal resolution of 1/3 arc-second and vertical accuracy (95% confidence interval) of 1.64 m (Gesch et al., 2014). Landcover classification based on NLCD 2011 (Homer et al., 2015) delineated the fully wetted zones (water) and intertidal zones (emergent herbaceous wetlands and woody wetlands).

*2.3. Variants of the model mesh*

The comprehensive mesh for the South Atlantic Bight, including all of its estuaries and marshes, was codenamed MARSH. Then the intertidal zones were removed from the MARSH mesh to generate the AIW mesh. Figure 1 displays the AIW mesh triangulation overlaid on the MARSH mesh extent for a zoomed-in view of the northeast Florida, Georgia and southeast South Carolina coastline. Next, the AIW (i.e., the proper waterway itself) was removed from the AIW mesh to generate the INLET mesh. Finally, the inlets were removed from the INLET mesh to generate the COAST mesh.

Table 3 lists details of the four meshes used in this study. The overarching concept of the four-mesh scheme is with the controlled way of including/excluding well-defined geophysical features (i.e., marsh, AIW and inlets/fully wetted estuarine zones) in the numerical simulations. The COAST mesh utilizes a hard coastline (i.e., there is no description of inshore features). The INLET mesh, which advances upon the COAST mesh by defining the inlets (64 total), estuaries, rivers and lagoons, where 62% of the total mesh nodes are used to describe the inshore features (4010 $km^2$ of surface area with size distribution 142 ± 109 m). The AIW mesh advances upon the INLET mesh by defining the AIW (i.e., the proper waterway itself), which in its entirety required ~45K mesh nodes, ensuring channel widths were resolved with no less than a span of three elements. The MARSH mesh, which advances upon the AIW mesh by defining the intertidal zones, where 86% of the total nodes are used to the describe the inshore features (7947 $km^2$ of surface area with size distribution 123 ± 89 m) and 56% of the inshore nodes are used to describe the intertidal zones (3672 $km^2$ of surface area with size distribution 119 ± 72 m). The intertidal zones in their entirety required ~225K mesh nodes, ensuring accurate representation of the marsh topography as well as sufficient description of the wetting and drying process.

*2.4. Simulation settings and model parameters*

The model simulations were spun up from a cold start with a forcing ramp applied to the first 10 days. A total of 45 days was simulated using a time step of 1.5 seconds. Boundary conditions included seven tidal constituents ($K_1$, $O_1$, $M_2$, $S_2$, $N_2$, $K_2$ and $Q_1$; see Hagen et al., 2006) on the open-ocean (60-degree west meridian) boundary and no-flux constraints on all other (mainland/island) boundaries. The global ocean model of Le Provost et al. (1998) defines the open-ocean boundary conditions. The momentum equations were solved in the generalized wave continuity formulation (Lynch and Gray, 1979) with the weighting factor (Kolar et al., 1994) set to 0.005 for still-water depth greater than 10 m, and 0.020 otherwise. Horizontal eddy viscosity was set to 5 $m^2 s^{-1}$ (Bunya et al., 2010). Bottom friction was characterized using spatially variant Manning's roughness based on landcover type: $n$ = 0.020 for fully wetted zones (water); $n$ = 0.035 for emergent herbaceous wetlands; and $n$ = 0.050 for woody wetlands. The critical step of parameterizing bottom friction based on the spatial variability of landcover character far outweighs the very limited sensitivity of the model regarding adjustment of horizontal eddy viscosity, at least within the range of 1–50 $m^2 s^{-1}$. Nonlinear finite amplitudes were enabled with the minimum allowable height for wetting and drying set to 0.1 m (Medeiros and Hagen, 2012). Nonlinear advection was enabled (Westerink et al., 2008). Geographical coordinates were used and Coriolis effects were enabled.

*2.5. Harmonic analysis and tidal resynthesis*

Harmonic analysis was applied to the last 30 days of simulated tides to determine the scalar- and vector-based (water levels and velocities, respectively) amplitudes and phases associated with 23 frequencies (refer to Giardino et al., 2011 for a full listing of the 23 tidal constituents employed by ADCIRC). To test the harmonic analysis procedure for the separation of astronomical constituents with nearly identical frequencies, the model was run over a length of 230 days with the last 185 days of simulated tides harmonically analyzed. The 185-day harmonic analysis was selected based on the limiting factor of the Rayleigh criterion, i.e., the minimum required record length for separating the $S_2$ (frequency = 0.000 145 $s^{-1}$) and $K_2$ (frequency = 0.000 146 $s^{-1}$) tidal constituents is ~183 days. In the end, the $S_2$ and $K_2$ tidal constituents were resolved virtually the same between the 30- and 185-day length of the harmonic analysis, where the constituent amplitudes turned out to be within a 0.005–0.007 m of each another and the constituent phases turned out to be within 2–3 degrees of each other. In this case, the Rayleigh criterion (a rule of thumb) was proven to be over-restrictive regarding the duration of the harmonic analysis, which is mainly due to the modeled tide signal being relatively very smooth with little to nil noise (Pugh and Woodworth, 2014—cf. page 74). Thus, the 45-day run length with 30-day length of harmonic analysis can be deemed sufficient for separation of the astronomical constituents with nearly identical frequencies, e.g., $K_2$ and $S_2$, as well as the extraction of shallow-water constituents, e.g., $M_4$ and $M_6$. Tidal resynthesis (Schureman, 1941) was utilized to reconstitute the full tidal signal from the 23 harmonically extracted tidal constituents. The tidal resynthesis was carried out over a tidal epoch (~18.6 years). Then tidal datums of HAT, MHHW, MHW, MSL, MLW, MLLW and LAT (Table 2) were evaluated from the 18.6-year-long time series of astronomical tide elevations.

## 3. Model skill assessment

Tidal data (MLW—mean low water, MHW—mean high water) were gathered for a total of 142 gaging stations in the South Atlantic Bight (refer to Figure 3a for the station locations).

The tidal datums of MLW and MHW were plotted as scatter for the estuary stations (129 total) of the South Atlantic Bight (Figure 3b). A quantitative comparison of observed and simulated MLW and MHW found the best-performing model results to be from the MARSH mesh ($R^2$ = 92%). For the MARSH model results, the root mean square error of the model-to-data fit was computed as 0.09 and 0.12 m for MLW and MHW, respectively. In running the same analysis on the AIW model results, the $R^2$ is 89% and root mean square error is 0.10 and 0.14 m (MLW and MHW). The MARSH model results show less bias in over-predicting the tidal datums (particularly MHW) relative to the AIW model results, which can be explained by the fact that the MARSH mesh permits for wetting and drying of adjacent intertidal zones during high tide, as opposed to the AIW mesh that constrains the flow in-bank and thus over-predicts high tide. Note the equations of the linear fits ($y = a + bx$) of the data-model results that show a lower intercept ($a$) and gentler slope ($b$) for the MARSH mesh ($a$ = 0.02 m and $b$ = 1.02 m m$^{-1}$) relative to the AIW mesh ($a$ = 0.05 m and $b$ = 1.09 m m$^{-1}$). The uncertainty in the data can be estimated to be 5 cm (Tamura et al., 2014), where the data-model fit was within the 5-cm data uncertainty for 62 of the 129 estuary stations (48%).

Of the total 129 estuary stations, only eight of them are located in partition 1 of the South Atlantic Bight (denser inlet-laden coastline from Winyah Bay, SC to the FL/GA border—cf. Table A1) (Figure 3a). The performance metrics based on the eight (partition 1) stations are not displayed on the scatter plots (Figure 3b), but: for the case of the MARSH mesh, the equation of the best-fit line is $y = -0.04 + 0.94x$, $R^2$ = 99% and MLW is near perfectly predicted, while MHW is generally under-predicted; and for the AIW mesh, the equation of the best-fit line is $y = -0.05 + 0.99x$, $R^2$ = 98% and both MLW and MHW are generally under-predicted. Of the 121 estuary stations associated with partition 2, a decent number of them are located in the St. Johns

River (as far upstream as 200 river km) and Indian River lagoon (as far as 100 km from the nearest tidal inlet), as representative of some of the more tidally damped regions of the estuaries. The model skill for the 121 estuary stations located in partition 2 of the South Atlantic Bight is: $R^2$ = 93% (MARSH); and $R^2$ = 90% (AIW).

Appendix B contains further presentation of the model skill assessment, including validation of fully resynthesized astronomical tides in the estuaries and tidal creeks.

## 4. Validation of shelf tidal circulation

For the evaluation of depth-integrated velocities, the vector-based tidal constituents were converted from astronomical parameters ($A_u$, $\varphi_u$, $A_v$ and $\varphi_v$, where $A$ stands for amplitude, $\varphi$ stands for phase and the $u$,$v$ subscripts stand for the easting and northing directions, respectively) to ellipse parameters (SEMA: semi-major axis, ECC: eccentricity, INC: inclination and PHA: phase) using the MATLAB routine ap2ep.m based on the rotary analysis of tides performed by Gonella (1972). Four gaging stations located on the continental shelf off the Georgia coastline (GR, R2, R5 and R6—refer to Figure 3a, inset) have tidal velocity data in the form ellipse parameters (Blanton et al., 2004). Station GR is the innermost shelf station in water depth of 15–20 m, stations R2 and R5 are both located at the 25-m bathymetric contour and station R6 is the outermost shelf station in water depth of 25–50 m. Based on the semi-diurnal nature of the tides in the South Atlantic Bight (Atkinson et al., 1985), in addition to the resonant geometry of the domain at the semi-diurnal tidal frequency (Battisti and Clarke, 1982), the $M_2$ tidal constituent is the variable of interest in this assessment. Table 4 lists the ellipse parameters for $M_2$ tidal velocities at the four shelf stations based on the data (Blanton et al., 2004) and four model results (COAST, INLET, AIW and MARSH). The semi-major axis values range from 0.25 (station GR) to 0.31 (station R2) m $s^{-1}$ among the four shelf gaging stations (see Figure 3a, inset for respective locations) according to the data, where the model (MARSH) replicates the observations near perfectly (within 0.01 m $s^{-1}$). The MARSH model results not only afford the best approximation of the semi-major axes, but also best-capture the shape (eccentricity), orientation (inclination) and timing (phase) of the $M_2$ tidal ellipses.

## 5. Impact of coastal features on shelf tides

Referring to Table 4, the semi-major axis values reveal an amplification of $M_2$ tidal velocities on the shelf due to the estuary-punctured coastline (i.e., AIW or INLET) versus an otherwise purely reflective boundary (i.e., COAST) à la Blanton et al. (2004). But, there is almost as measurable an impact on continental-shelf $M_2$ tidal velocities with the intertidal zones (i.e., MARSH), albeit in a negative-amplification sense (i.e., decay). It is also notable that the AIW has minor impact on shelf tidal circulation (i.e., AIW vs. INLET), although the AIW does have a substantial impact on local estuarine tidal circulation (e.g., refer to Bacopoulos and Hagen (2009) for study of the Loxahatchee River in southeastern Florida). Regarding the phase of the tidal ellipses, increasing geophysical description of the South Atlantic Bight within the mesh (i.e., COAST → INLET → AIW → MARSH; see Table 3 for details of the four meshes) generates further phase lag with the simulated tidal ellipse, where the best agreement with the data (278.5–289.6°) was achieved by the MARSH mesh (273.8–285.9°). This same trend is found with inclination (data 144.5–149.2° and MARSH 155.1–156.0°) and for the most part eccentricity (|data| 0.269–0.363 and |MARSH| 0.213–0.350).

Discerning the results of semi-diurnal ($M_2$) velocities (Table 4), the semi-major axes for the case of AIW ÷ COAST relate to ratio values of 1.12–1.25 among the four shelf gaging stations, which being greater than 1 indicate tidal amplification. The inshore features of the coastline clearly promote an amplification of $M_2$ tidal velocities on the shelf, as was similarly shown by Blanton et al. (2004). Further, the increasing phase of $M_2$ tidal velocities with progressively added geophysical features of the coastline adjusts the water level-velocity phase relationship on the continental shelf to bring the system's standing wave dynamics closer to resonance. To the contrary, the semi-major axes for the case of MARSH ÷ AIW result in ratio values of 0.93–0.98, which being less than 1 indicate tidal decay. The intertidal zones clearly generate a decay of $M_2$ tidal velocities on the shelf. Note that the four shelf gaging stations are located in partition 1, i.e., the more inlet- and marsh-dense coastline of the South Atlantic Bight (Table A1). The apparent tidal amplification and decay are analyzed in greater detail, including geographic partitions 1 vs. 2 of the South Atlantic Bight, in the next sub-sections of the paper.

### *5.1. Influence of estuarine/riverine features on shelf circulation*

The AIW model results were compared with the COAST model results on a domain-wide basis to isolate the impact of the (fully wetted) estuarine/riverine features on shelf circulation. Figure 4 displays spatial fields of $M_2$ velocity tidal amplification based on the AIW vs. COAST model results for the entire South Atlantic Bight with zoom-in views of partition 1 and the Altamaha and St. Mary's Rivers. Tidal amplification refers to the ratio of the $M_2$ velocity amplitudes (i.e., semi-major axes—AIW ÷ semi-major axes—COAST): values >1 relate to amplification; and values <1 relate to decay. The response is mostly concentrated in partition 1 of the South Atlantic Bight, with little to no response in partition 2 due to the limited number of (small-sized) tidal inlets to 'open' the coastline, coupled with the fact that there are large (dissipative) lagoonal systems expanding throughout the back bays (Table A1), but more so that the continental shelf is narrow in relation to the shelf width for partition 1 (Figure 1). For partition 1, ratio values (tidal amplification) in the South Atlantic Bight range from 1.05–1.1 along the shelf break to 1.25–1.5 along the coastline and 2 or greater at the mouths of the inlets (e.g., 5–10 at Altamaha and St. Mary's). The response is greatest along the coastline, especially in the vicinities of tidal inlets, but the offshore scale of the response over the continental shelf, and even beyond the break, is remarkable given the physical mechanism of semi-diurnal ($M_2$) co-oscillation of standing waves (resonance) between the shelf and the deep ocean (Redfield, 1958). Like the co-oscillation of shelf tides with deep-ocean tides, there is a similar positive feedback between the coastal/estuarine tide and the shelf tide, whereby together the natural frequency of the system is brought closer to resonance with the semi-diurnal ($M_2$) tide. The size and density of the inlets along partition 1 of the South Atlantic Bight is the casual factor of the tidal amplification on the regional shelf, since they generate an 'openness' of the coastline (i.e., tidal prism) to effectively extend the continental shelf width and reinforce the already resonant $M_2$ tidal motions. There are two positive feedbacks responsible for amplified/unamplified tides in the South Atlantic Bight: 1) the shelf width is widest in partition 1 and relatively narrow for partition 2; and 2) the inlets are largest and densest along partition 1 and relatively limited and small for partition 2. For partition 1, the continental shelf is widest and there are also many sizable inlets punctuating the coastline, thus leading to regionally amplified tidal velocities of the $M_2$ frequency.

We consider resonance/effective shelf width (i.e., continental margin theory; refer to Clarke and Battisti, 1981) as an explanation for the tidal amplification of $M_2$ shelf circulation caused by the inlets and estuarine rivers. Five cross-shelf transects were drawn from the coastline to the shelf break for partition 1 of the South Atlantic Bight, as displayed in Figure 4a:

Charleston Harbor, SC; Edisto River, SC; Savannah River, GA; Altamaha River, GA; and St. Mary's River, FL. The shelf widths for the five transects are 104, 124, 134, 135 and 126 km, while the effective shelf widths (i.e., a proxy for the shelf width obtained by adding the inshore river distance) are 134, 182, 164, 179 and 163 km. The inshore river distance does not necessarily correspond to the total distance of the river, but instead it is based on the length of river course up to the tidal limit (where the tidal amplitude ceases to be 10 cm). Scale factors (see $v$ in Eq. 1) for the shelf widths are 0.08, 0.12, 0.14, 0.14 and 0.13 for the five transects, while the corresponding $v$ values for the effective shelf widths are 0.14, 0.25, 0.21, 0.25 and 0.21. Ratios of the scale factors (i.e., $v$-effective versus $v$-standard) are 1.69, 2.16, 1.51, 1.77 and 1.67 for the five transects, while the corresponding tidal amplification is 1.82, 2.04, 1.73, 1.68 and 1.71. For the case of the modeled $M_2$ velocity, the transect values of tidal amplification were computed by interpolating the spatially based fields of $M_2$ semi-major axes (AIW ÷ COAST) to the transects and applying an equal-weighted average to the transect points per transect (Figure 5). The similarity between the scale factors (as a function of the shelf width vs. the effective shelf width) and the tidal amplification of $M_2$ velocities (AIW ÷ COAST) suggests that astronomic tides in the South Atlantic Bight are, at least to an extent, governed by continental margin theory. The coastline of the South Atlantic Bight for partition 1 is punctuated by numerous, large tidal inlets that service long rivers in the back bays (Table A1). The shelf width, which is already at its widest point in the South Atlantic Bight, is effectively extended by the 'openness' of the coast and the connectedness to elongated estuarine/riverine systems. The coastline, inlet and inshore features of partition 1 contribute to the effective shelf width, which brings the system closer to resonance with the semi-diurnal ($M_2$) tidal frequency (Redfield, 1958) and results in a regional amplification of tidal velocities.

*5.2. Influence of the intertidal zones on shelf circulation*

The MARSH model results were compared with the AIW model results on a domain-wide basis to isolate the impact of the intertidal zones on shelf circulation. Figure 6 displays spatial fields of $M_2$ velocity tidal decay based on the MARSH vs. AIW model results the entire South Atlantic Bight with zoom-in views of partition 1 and the Altamaha and St. Mary's Rivers. Tidal decay refers to the ratio of the $M_2$ velocity amplitudes (i.e., semi-major axes—MARSH ÷ semi-major axes—AIW): values <1 relate to decay; and values >1 relate to amplification. Like the case of tidal amplification (Figure 4), the response of tidal decay is predominantly located in partition 1 of the South Atlantic Bight. For partition 2, the tidal decay is essentially nil. Referring to the geographic site assessment of the South Atlantic Bight (Table A1), there is a total of 3300 $km^2$ of intertidal zones for partition 1, and only a fraction of that for partition 2 (400 $km^2$). As evidenced, the intertidal zones are a responsible factor of the tidal decay. For partition 1, ratio values (tidal decay) are 0.98–0.99 along the shelf break, 0.8–0.9 at the mouth of the Altamaha River and 0.75–1.05 at the mouth of the St. Mary's River. The response is greatest in front of the Altamaha River and similarly substantial in front of the St. Mary's and St. Johns Rivers. Peculiarly, there are *hot spots* of tidal amplification (>1), which we propose to be the result of over-/under-compensation of the local tidal velocities to account for the presence/absence of the intertidal zones. However, these *hot spots* are localized with respect to the offshore scale of the response (tidal decay) over the shelf. As would be expected, the tidal dynamics of the inshore waters are dampened by the intertidal zones, but it is astonishing that the tidal decay extends offshore and over the continental shelf, and even goes past the break. The 'open' coastline of partition 1, because of the many punctuating inlets, and the expansive intertidal zones populating the back bays are the causal factors for the regionally decayed tidal velocities of the $M_2$ frequency.

We consider bottom stress and the associated energy dissipation for explanation of the tidal decay of $M_2$ shelf circulation caused by the intertidal zones. The bottom friction terms of the momentum equations (see Westerink et al., 2008 for the full form of the shallow-water equations used in ADCIRC) are quadratic functions of the local velocity:

$$a_{\mathrm{bot}-\lambda} = U\frac{C_f\sqrt{U^2+V^2}}{H} \quad \text{and} \quad a_{\mathrm{bot}-\phi} = V\frac{C_f\sqrt{U^2+V^2}}{H} \qquad \text{(2a and 2b)}$$

where $a_{\mathrm{bot}}$ stands for acceleration due to bottom friction, $U$ and $V$ are the depth-integrated velocities in the longitudinal ($\lambda$) and latitudinal ($\phi$) directions, respectively, $H$ is the height of the local water column and $C_f$ is the bottom friction coefficient:

$$C_f = \frac{g}{H^{1/3}}n^2 \qquad (3)$$

where $g$ is gravity and $n$ is the Manning's $n$ coefficient (units of s $m^{-1/3}$). Bottom stress was calculated for the fully wetted zones and flooded intertidal zones from modeled spatial fields of depth-integrated velocities and water surface elevations:

$$\tau_{\mathrm{bot}-\lambda} = \rho H a_{\mathrm{bot}-\lambda} \quad \text{and} \quad \tau_{\mathrm{bot}-\phi} = \rho H a_{\mathrm{bot}-\phi} \qquad \text{(4a and 4b)}$$

where $\tau_{\mathrm{bot}}$ stands for stress due to bottom friction and $\rho$ is the density of seawater. To convert the vector quantity of bottom stress to a scalar quantity of work/energy, we diagnosed energy dissipation based on a cubic function of the $M_2$ tidal velocity-ellipse field over a tidal period:

$$E_{\mathrm{bot}} = \frac{1}{T}\int_{t_0}^{t_0+T}\left[\tau_{\mathrm{bot}-\lambda}(t)^2 + \tau_{\mathrm{bot}-\phi}(t)^2\right]^{3/2}dt \qquad (5)$$

where $E_{\mathrm{bot}}$ is the $M_2$ tidal energy dissipation rate (units of W $m^{-2}$) and $T$ is the $M_2$ tidal period (0.518 days). Integrals of energy dissipation rates were computed as $P_{\mathrm{bot}} = \iint_A E_{\mathrm{bot}} dA$, where the area of integration $A$ was variably chosen as the entire South Atlantic Bight coastline (extending offshore to the 100-m bathymetric contour—consistent with Blanton et al., 2004), the intertidal zones alone, the Altamaha River and the St. Mary's River.

Figure 7 displays spatial fields of bottom stress based on the MARSH model results for a characteristic spring tidal cycle (i.e., semi-diurnal frequency—$M_2$) in the South Atlantic Bight. $M_2$ tidal energy dissipation in the South Atlantic Bight is 0.001–0.01 W $m^{-2}$ along the shelf break and oceanward, 0.02–0.05 W $m^{-2}$ over the continental shelf and 0.5–5 W $m^{-2}$ in the lower reaches of the estuarine rivers and inlet throats. Note the large extent of inundation within the intertidal zones (e.g., Altamaha and St. Mary's), where bottom stress is for the most part 0.05–1 W $m^{-2}$. Integrating bottom stress over the entire South Atlantic Bight coastline (i.e., energy dissipation—$P_{bot}$) amounts to 1.97 GW (Blanton et al., 2004 report 1.6 GW—no intertidal zones), while 29% of the total energy dissipation occurs in the intertidal zones, and for the Altamaha River amounts to 64 MW (59% occurring in the local intertidal zones) and for the St. Mary's River amounts to 33 MW (38% occurring in the local intertidal zones). Albeit a portion of the overall tidal energy dissipation is due to the enhancement of the standing ($M_2$) wave dynamics/resonance and shelf tidal velocities because the inshore features are resolved (Blanton et al., 2004), there is a near-equal contribution to the overall tidal energy dissipation caused by the shallow flows occurring over the intertidal zones during high waters of the tidal cycle. In summary, the intertidal zones are a predominant factor towards the $M_2$ tidal energy dissipation occurring in the South Atlantic Bight.

## 6. Discussion

*6.1. Scope of the modeling approach and tidal physics*

The modeling approach (ADCIRC) employed in the present study assumes depth-integrated circulation and accounts for barotropic tidal flow physics (shallow-water equations). Baroclinic effects are not considered in the tidal simulations herein for the South Atlantic Bight. Future modeling study involving baroclinic dynamics on the South Atlantic Bight shelf, namely stratification of flow velocities within the vertical water column, will require a comprehensive upstream forcing that is representative of the region-wide distribution of the river discharge (Aretxabaleta et al., 2007). As another matter of future work, the resonance of the $M_2$ tide in the South Atlantic Bight and the potential modulation by other tidal constituents (Kowalik and Polyakov, 1998) requires investigation. For example, the combination of the $M_2$ and $S_2$ constituents (both of which are amplified in the South Atlantic Bight due to semi-diurnal dynamic resonance, yet having nearby frequencies) can generate beat-type irregularities in the astronomical tides (Maas and Doelman, 2002). Moreover, astronomical tides, including the $M_2$ tidal constituent, can be susceptible to nodal variations (18.61- and 8.85-year cycles) and long-term (secular) changes (Feng et al., 2015).

*6.2. Tidal datums inside the estuaries as a function of the intertidal zones*

The most reliable measures of tidal datums are those derived from *in-situ* observations (e.g., National Oceanic and Atmospheric Administration—cf. NOAA Tides and Currents, 2015). However, the observation stations are usually sparsely located relative to the larger geographic region of interest, e.g., only 129 estuary stations cover the entire coastline of the South Atlantic Bight. Stations with tidal datums calculated from observed data are typically very limited inside the estuarine rivers and tidal creeks, e.g., only eight of the estuary stations were located in partition 1 of the South Atlantic Bight. Tools like VDatum (Parker et al., 2003) provide regional maps of tidal datums that cover the estuaries, where such tools are primarily based on hydrodynamic models that represent the open-water zones of the estuaries. While the models supporting such tools are highly refined and validated for their given region(s), they commonly do not describe and account for tides and tidal flows occurring in the intertidal zones (e.g., see Yang et al., 2012 for reporting of tidal models in support of VDatum for the South Atlantic Bight). There is 'mathematical' justification for excluding the intertidal zones from tools that provide regionally based tidal datums (e.g., VDatum—cf. Vertical Datum Transformation, 2016). For example, the intertidal zones would experience periodic high waters from which MHW, MHHW and HAT can be assessed, but the signal would dry out during low waters, thus prohibiting the calculation of MLW, MLLW, LAT and MSL. Contrariwise, there is 'physical' relevance of the tidal datums within the intertidal zones. The environment and ecology of the intertidal zones have direct ties to the local tidal datums (e.g., see McKee and Patrick, 1988 for a review of the relationship of *Spartina alterniflora* to tidal datums). As well, secular trends have been uncovered in tidal datums (e.g., see Flick et al., 2003 for evaluation of the United States). To that end, our simulation of tides and calculation of tidal datums throughout such an expansive marsh indicates that the hydroperiod over the marsh surface is being established by the numerical model. Such a capability has great potential for establishing bio-geo-physical models, but that is for future efforts.

*6.3. The underlying importance of geometry*

$M_2$ tidal velocities in the South Atlantic Bight are in resonance due to the geometry of the ocean basin (i.e., shelf depth and width) and the resulting standing wave dynamic is at the semi-diurnal frequency. However, the geometry of the coastline is an added influencing factor of $M_2$ tidal velocities in the South Atlantic Bight. The shelf is widest at the Florida/Georgia border, where the coastline is also heavily punctuated by tidal inlets and the back bays are populated by long, interconnected rivers that are surrounded by expansive intertidal zones. The system resonance is affected by the coastline definition by way of effectively extending the shelf width to enhance the foregoing standing wave dynamics. Furthermore, the convergent-shaped estuaries constitute an added geometric feature to the coastline causing an amplification of the tide. Overall, the tidal boundary is extended inshore beyond the physical coastal boundary due to the dense inlet-river character of the coastline, while the resulting extension of the (effective) shelf width reinforces the already-resonant $M_2$ tidal velocities of the South Atlantic Bight. The tidal prism afforded by the dense estuarine features of the coastline should also be a considering factor in defining the general reflectivity of the coastal boundary and/or the location of the coastal boundary from a tidally reflective standpoint. The intertidal zones contribute to the tidal prism by way of increasing the storage capacity of the estuaries, but they also act as momentum dissipaters and increase the overall tidal energy dissipation of the system, thus decaying $M_2$ tidal velocities at the offshore scale over the continental shelf. Considering everything, the geophysical features influencing astronomic tides in the South Atlantic Bight are the depth and width of the continental shelf and the definition of the coastline, including: tidal inlets (size and density along the coast); estuaries (type and shape); conjoining rivers (lengths); and intertidal zones (surface area). Notably, the variables for these geophysical features are fundamentally geometric. Dynamically, the standing wave behavior (resonance) of astronomic tides in the South Atlantic Bight is a function of the shelf and coastline geometries.

*6.4. Comparison with other studies of tidal circulation in large-scale interconnected systems*

A similar study of shelf circulation for the South Atlantic Bight is that performed by Blanton et al. (2004), where they discovered an amplification of the tidal velocities over the continental shelf due to the presence of the inshore (estuarine) features of the coastline, i.e., the open-water features. Here, we have demonstrated the same impact (tidal amplification) of the estuarine (open-water) features of the coastline. But, we have also shown the intertidal zones of the estuaries to be a contributing factor of the coastline definition and its influence on shelf circulation (tidal decay). The underlying concept is that the intertidal zones generate an added storage capacity and introduce new regions of dissipation, which (subtly) modifies the mode of tidal propagation and tidal amplitudes in the South Atlantic Bight. Comparable findings of subtle changes in tidal amplitudes due to increased tidal extent and energy dissipation, as subject to sea-level rise, have been observed for the European Shelf (Pelling et al., 2013). The theme of comprehensively defining the estuarine and intertidal features of the coastline, as implemented here for the estuaries and intertidal zones of the South Atlantic Bight, is similar to other contiguous-domain modeling studies (e.g., see Khangaonkar et al., 2017 for assessment of circulation and inter-basin transport in the Salish Sea including Johnstone Strait and Discovery Islands pathways). For some additional perspective, the present modeling study for the South Atlantic Bight is also like other recent works that have modeled tidal propagation in a computational domain stretching from the limit of tidal influence (in a tidal river network) to the shelf break, or beyond, including: the finite-element, multi-scale model of the Scheldt tributaries, river, estuary and region of freshwater influence by de Brye et al. (2010); the unstructured-mesh modeling of the Congo river-to-sea continuum by Le Bars et al. (2016); and simulations of the flow in the Mahakam river-lake-delta systems, Indonesia by Van et al. (2016). Modeling the system as a continuous whole captures the interconnectedness of the hydrodynamics and provides a basis for multi-process simulation in support of resilience and mitigation evaluation (e.g., see Robins et al., 2016).

Coastlines with intricate features, e.g., estuaries, rivers, intracoastal waterways, intertidal zones, straits, island pathways, tributaries, anabranches and other like channels, generate an interconnectedness of the inshore and offshore waters and the circulation, which additionally (although subtly) modifies the mode of tidal propagation and tidal amplitudes over the continental shelf. As well, coastline promontories and indentations can generate a boundary effect on shelf circulation (e.g., the Grande Bay and San Jorge Gulf, Southwestern Atlantic Shelf—cf. Palma et al., 2004). Even bathymetric features along the coast can impact barotropic tidal flows at the shelf scale (e.g., the Nantucket shoals impacting regional tidal dynamics in the New England shelf—cf. Shearman and Lentz, 2004). The coastal regions, including the intricate estuarine and intertidal features, require detailed topography and associated mesh sizes no greater than a 0.5-km scale for shelf-scale resolution of the $M_2$, $M_4$, $M_6$, $S_2$, $N_2$, $K_1$ and $O_1$ tides (e.g., the west coast of Britain and the Irish Sea—cf. Jones and Davies, 2007). We suggest that a 10-m scale for mesh/grid size of the coastline features is necessary for sufficient geometric-dynamic capture of the domain and physics. Our work indicates that shelf-scale hydrodynamic modeling and assessment should consider the domain as a contiguous whole, including a high-resolution definition of the complex estuarine and intertidal facets of the coast.

## 7. Summary and conclusions

Barotropic, depth-integrated tides in the South Atlantic Bight were simulated (shallow-water equations, specifically Advanced Circulation—ADCIRC) using a high-resolution (~10 m), unstructured triangular mesh that describes the full inshore features of the coastline at an unprecedented level of definition. Regional maps of tidal datums (HAT, MHHW, MHW, MSL, MLW, MLLW and LAT; refer to Table 2 for definitions and descriptions) were generated for the entirety of the South Atlantic Bight with local details (resolution of 10–100 m) of the estuaries and intertidal zones. The physics of the various coastal features, including the inlets, estuarine rivers, Atlantic Intracoastal Waterway and intertidal zones, and their associated impact on local (estuarine) and regional (shelf) circulation, were carefully investigated using methodical variations of the high-resolution mesh. The comprehensive mesh for the South Atlantic Bight (codenamed MARSH) describes the entirety of the fully wetted regions (4275 km$^2$, including 64 tidal inlets, 40 estuarine rivers and the contiguous Atlantic Intracoastal Waterway) and intertidal zones (3672 km$^2$, including tidal flats and salt marshes). Three byproduct meshes were developed from the MARSH mesh, including AIW (MARSH minus intertidal zones), INLET (AIW minus Atlantic Intracoastal Waterway) and COAST (INLET minus inlets, rivers and lagoons), such that the influences of the various geophysical features on shelf and estuarine circulation were examined in complete isolation.

The model was rigorously validated against tidal data at 142 gaging stations ranging over the estuaries, open coast and continental shelf of the South Atlantic Bight. The MARSH model performed at $R^2$ = 92% in simulating mean lower water (MLW) and mean high water (MHW) at 129 estuary gaging stations. Inclusion of the wetting and drying of the intertidal zones was influential in more accurately capturing high tide, i.e., when compared with the artificially (elevated) bank-constrained high tide simulated by the AIW model ($R^2$ = 89%), which was especially evident at 16 tidal-creek gaging stations and most evident at two marsh gaging stations. In addition to MLW and MHW, the nuances of the tide, including the spring-neap variation and diurnal inequality, were captured within 10% error when compared with observed data. The MARSH model captured $M_2$ velocities over the continental shelf within 0.01 m $s^{-1}$ error when compared with observations at four shelf gaging stations. The intertidal zones are an important geometric feature regarding astronomic tides in the estuaries of the South Atlantic Bight as well as over the continental shelf.

Tidal mechanics associated with the resonance of the semi-diurnal ($M_2$) frequency are influenced by the inlets and estuarine rivers of the South Atlantic Bight coastline. The effective shelf width (i.e., shelf width plus inshore river distance) is the responsible factor of the $M_2$ tidal amplification occurring over the continental shelf. The tidal amplification generated by the model (i.e., MARSH vs. AIW) was near identical to that predicted by continental margin theory (i.e., resonance scale factor vs. effective shelf width). The numerous estuarine rivers located from northeast Florida to southeast South Carolina (many of which are convergent in shape) effectively extend the shelf width and reinforce the resonance of the $M_2$ tide. Tidal mechanics associated with the momentum dissipation of the tidal circulation are influenced by the intertidal zones of the South Atlantic Bight estuaries. The wetting and drying of the intertidal zones is responsible for the $M_2$ tidal decay occurring over the continental shelf. Of the total amount of $M_2$ tidal energy dissipation that occurs in the South Atlantic Bight (1.97 GW), approximately one third of it occurs in the intertidal zones. The dissipation of momentum caused by the tidal inundation of the intertidal zones impacts the shelf circulation in a decay sense.

Astronomic tides in the South Atlantic Bight are dominated by the $M_2$ frequency, which are in a resonant mode due to the geography (i.e., latitude) and geometry (i.e., shelf width) of the domain. The estuarine and intertidal definition of the South Atlantic Bight coastline (subtly) modifies the mode of tidal propagation, and associated resonant properties, over the continental shelf. This study confirms the tidal inlets and estuarine rivers of the South Atlantic Bight coastline to positively impact the $M_2$ resonance because of effective shelf width. The floodplains and marshes negatively impact the $M_2$ tidal circulation because of bottom friction and energy dissipation. Wetting and drying (i.e., tidal inundation), nonlinear bottom friction and nonlinear advection are all important factors of tides in the South Atlantic Bight. This study demonstrates the necessity of a complete geometric and dynamic description of the domain/physics for adequate numerical (tidal) simulation.

## Appendix A. Geographic site assessment of the South Atlantic Bight

Straight-line distance between Cape Hatteras, North Carolina and West Palm Beach, Florida measures 1000 km in length (Figure A1). The general curvature of the South Atlantic Bight coastline measures 1300 km in length. Considering the high-definition curvature of the South Atlantic Bight coastline, including all open coast, river and island boundaries, it measures 19,000 km in total length (NOAA Office for Coastal Management, 2017). Just by linear measure of coastline distance, the estuaries and marshes of the South Atlantic Bight present a highly complex geometry. In fact, there is an apparent fractalization of the South Atlantic Bight coastline, where the bounding length is a function of the measurement resolution, i.e., the fractional dimension (Mandelbrot, 1967), which exemplifies the ‘coastline paradox’ of bounding a finite region with an infinitely long boundary due to the complexity of coastline definition.

The 64 inlets of the South Atlantic Bight can be split into two partitions (Figure A1). The first partition includes 27 inlets along 350 km of coastline from the Florida/Georgia border to Winyah Bay, South Carolina, with average inlet width of 2900 m and average coastline distance between adjacent inlets of 15 km (Table A1). The second partition includes 37 inlets along 950 km of coastline for Florida's east coast, the northern portion of South Carolina and North Carolina, with average inlet width of 600 m and average coastline distance between adjacent inlets of 26 km. The 27 inlets of the first partition are wider than the 37 inlets of the second partition by a factor of 4.5, while also being more densely populated along the coastline by a factor of 1.7. The cross-sectional area (width × depth) of the 27 inlets of the first partition averages 8600 $m^2$ (total 232,000 $m^2$), which compares with 2200 $m^2$ for the 37 inlets of the second partition (total 76,000 $m^2$). Considering a near linear relationship between tidal prism and inlet cross-sectional area (Keulegan, 1967; Jarrett, 1976), it can be estimated that there is roughly three times more tidal flux/exchange for the Georgia/southeast South Carolina coastline relative to the Florida/northeast South Carolina/North Carolina coastline by comparing the total cross-sectional area of the 27 inlets of the first partition with that for the 37 inlets of the second partition: $232{,}000 \text{ m}^2 \div 76{,}000 \text{ m}^2 \approx 3.05$.

The estuaries of the South Atlantic Bight can be categorized based on shape according to convergent (funnel-shaped), prismatic or divergent (bay-shaped) (refer to Savenije, 2012 for description of each classification) (Table A1). There are 9 convergent, 8 prismatic and 0 divergent estuaries for the Georgia/southeast South Carolina coastline, where the convergent estuaries include Charleston Harbor, St. Helena Sound, Wilmington and Ogeechee Rivers, Blackbeard and Fancy Bluff Creeks, and Satilla, St. Mary's and Nassau Rivers (Figure A1). There are 5 convergent, 7 prismatic and 6 divergent estuaries for the Florida/northeast South

Carolina/North Carolina coastline, where the divergent estuaries include Bogue Sound, Banks Channel/Virginia Creek/AIW, Indian River and Lake Worth Lagoons, and Biscayne Bay. The Georgia/southeast South Carolina coastline (where the continental shelf is widest) is dominated by convergent-shaped estuaries, while the Florida/northeast South Carolina/North Carolina coastline (where the continental shelf is narrowest) is dominated by divergent-shaped estuaries.

The estuaries and rivers of the South Atlantic Bight can also be categorized based on type according to coastal plain, piedmont or barrier islands (refer to Dame et al., 2000 for description of each classification) (Table A1). Some of the more prominent rivers of the South Atlantic Bight coastline include the Waccamaw River (90 km stream length), Santee River (60 km), Cooper River (45 km), Altamaha River (50 km), St. Mary's River (40 km) and St. Johns River (200 km) (Figure A1). For the Georgia/southeast South Carolina coastline, there are 9 coastal plain-type estuaries/rivers, 6 piedmont-type and 3 barrier island-type. For the Florida/northeast South Carolina/North Carolina coastline, there are 5 coastal plain-type estuaries/rivers, 2 piedmont-type and 11 barrier island-type. The Georgia/southeast South Carolina coastline (where there are wide expanses of salt marsh) is dominated by coastal plain-type estuaries/rivers, while the Florida/northeast South Carolina/North Carolina coastline (where there are numerous and large lagoons) is dominated by barrier island-type estuaries/rivers.

Salt marshes consisting primarily of *Spartina alterniflora* and *Juncus roemerianus* grass species dominate the estuaries from the Florida/Georgia border to Winyah Bay, South Carolina, while mangrove wetlands and seagrasses populate the estuaries of central and southeast Florida (Dame et al., 2000). For the Georgia/southeast South Carolina coastline, there is a total of 3300 $km^2$ of marshland (Table A1), including the marsh systems between Bulls Bay and Sapelo Island NERR, while for the Florida/northeast South Carolina/North Carolina coastline, there are only

400 km$^2$ of marshland, which is made up of the Waccamaw National Wildlife Refuge, North Inlet-Winyah Bay NERR, Timucuan Preserve and Guana-Tolomato-Matanzas NERR (Figure A1). For the northern and southern portions of the South Atlantic Bight coastline, there are five lagoons totaling 2200 km$^2$ in surface area. Notable lagoonal systems include the Indian River Lagoon and Biscayne Bay, located in central and south Florida, respectively. The Indian River Lagoon is serviced by Ponce de Leon, Sebastian, Fort Pierce and St. Lucie Inlets. Biscayne Bay has an open entrance to the ocean with additional open-ocean connections via Bakers Haulover, Government, Norris and Bear Cuts.

## Appendix B. Comprehensive model skill assessment

Figure B1 displays data vs. modeled (MARSH) MLW and MHW for the 129 estuary stations of the South Atlantic Bight. The data and model results exhibit a discernible spatial variation of tidal datums in the South Atlantic Bight, including: 1) at the regional scale, the largest tides are experienced at Georgia and north Florida, while the tidal range gets smaller going north (South Carolina and North Carolina) and south (central and south Florida) along the coastline; and 2) at the local scale, the largest tides are experienced at the open coast/river mouth and AIW, while the smallest tidal ranges are deep (upstream) into the riverine/lagoonal systems (e.g., St. Johns River and Indian River lagoon). The largest tidal ranges just exceed 2 m, as defined by MLW and MHW of the data and model results, while the smallest tidal ranges get as low as mere centimeters in upper river reaches and within lagoons. The largest tidal ranges occur for the three stations located in Georgia, which is representative of partition 1 of the South Atlantic Bight (Table A1), where the continental shelf is widest and the semi-diurnal ($M_2$) tide is resonant (Redfield, 1958; Blanton et al., 2004). The model results accurately capture the spatial variation of tidal datums in the South Atlantic Bight as described by the data. The tidal-datum charts reveal an extraordinary skill (performance) of the model to simulate astronomic tides in the South Atlantic Bight and its estuaries and intertidal zones.

Of the 129 estuary stations for the South Atlantic Bight, 16 are located in a tidal creek (i.e., a tidally influenced stream that extends off the main river branch and into marsh, mudflat and/or higher topography). The tidal-creek gaging stations (Figure 2) range regionally from as far north as North Inlet-Winyah Bay (South Carolina) to as far south as the Loxahatchee River (Florida) and locally among coastal (1–5 km distance from the nearest inlet mouth), AIW (9–33 km distance from the nearest inlet mouth) and river/lagoon (14–150 km distance from the nearest inlet mouth). The tidal signals for the 16 tidal-creek gaging stations were reconstituted for the first 14.77 days (spring-neap tidal cycle) of a tidal epoch (Figure B2), where the model results shown are those from the best-performing mesh (MARSH). The tidal plots show excellent agreement between the data and model results, although there is some imperfection with the capture of the spring tidal amplitudes at some of the stations, e.g., indexes 1–3, 8 and 14. The overall RMSE for the MARSH model results was 9.9 cm, compared with an overall RMSE of 10.3 cm for the AIW model results.

Of the 16 tidal-creek gaging stations, two are located in a marsh (Timucuan Preserve—cf. Figure 2): Sisters Creek—AIW; and Clapboard Creek—St. Johns River. The greatest improvement in the model results (i.e., AIW → MARSH) was achieved at these two marsh stations, where $RMSE_{AIW}$ (15.5 cm) was reduced by 0.9 cm (6%) with the MARSH mesh (RMSE = 14.6 cm) for Sisters Creek and $RMSE_{AIW}$ (10.7 cm) was reduced by 1.1 cm (10%) with the MARSH mesh (RMSE = 9.6 cm) for Clapboard Creek. Figure B3 shows parametric tide plots and tidal charts for spring and neap tides at Sisters Creek and Clapboard Creek. The parametric tide plots are in polar space ($r$, $\theta$), where the angle ($\theta$) rotates counter-clockwise over a full period (one day), which almost captures two full tidal cycles, and the signage (+/–) of the radius ($r$) is retained. The plots and charts illustrate the spring-neap variation of the tides (spring tidal range is ~2 m and neap tidal range is ~0.75 m) and the markedly more diurnal inequality for high water (HHW is greater than HW by 0.1–0.5 m) than low water (LLW is less than LW by 0–0.1 m). The model captures these features of the tide at both stations.

**Acknowledgements**

The authors thank Peter Sucsy of the St. Johns River Water Management District (SJRWMD), Gordon Hu of the South Florida Water Management District (SFWMD), Amy Kalmbacher of the Florida Department of Environmental Protection, Steven Bratos of the United States Army Corps of Engineers and David Scharff of the National Oceanic and Atmospheric Administration (NOAA) for providing the bathymetric and hydrodynamic data used in this study. Thanks to Matthew Bilskie for providing help in preparing the paper. Funding was in part under Award No. DUE0525429 from the National Science Foundation, Award No. N00014-02-1-0150 from NOAA and the U.S. Department of Commerce, Contract No. SK91912 from SJRWMD, Contract No. 4500019382 from SFWMD, the NASA Kennedy Space Center, Ecological Program, Climate Adaptation Science Investigators project—Award No. IHA-SA-13-006 and the Louisiana Sea Grant Laborde Chair Endowment. This paper is dedicated to Peanut Bacopoulos (R.I.P. July 21, 2016).

## References

Alizad, K., Hagen, S.C., Morris, J.T., Bacopoulos, P., Bilskie, M.V., Weishampel, J.F., Medeiros, S.C., 2016. A coupled, two-dimensional hydrodynamic-marsh model with biological feedback. Ecological Modelling 327, 29–43.

Aretxabaleta, A., Blanton, B.O., Seim, H.E., Werner, F.E., Nelson, J.R., Chassignet, E.P., 2007. Cold event in the South Atlantic Bight during summer of 2003: Model simulations and implications. Journal of Geophysical Research 112, doi: 10.1029/2006JC003903.

Atkinson, L.P., Menzel, D.W., Bush, K.A., 1985. Oceanography of the southeastern U.S. continental shelf. Coastal and Estuarine Sciences, Volume 2. American Geophysical Union, Washington, DC, 156 pp.

Bacopoulos, P., Hagen, S.C., 2009. Tidal simulations for the Loxahatchee River estuary (southeastern Florida): On the influence of the Atlantic Intracoastal Waterway versus the surrounding tidal flats. Journal of Waterway, Port, Coastal and Ocean Engineering 135, 259–268.

Bacopoulos, P., Hagen, S.C., Cox, A.T., Dally, W.R., Bratos, S.M., 2012. Observation and simulation of winds and hydrodynamics in St. Johns and Nassau Rivers. Journal of Hydrology 420–421, 391–402.

Bacopoulos, P., Parrish, D.M., Hagen, S.C., 2011. Unstructured mesh assessment for tidal model of the South Atlantic Bight and it estuaries. Journal of Hydraulic Research 49, 487–502.

Battisti, D.S., Clarke, A.J., 1982. A simple method for estimating barotropic tidal currents on continental margins with specific application to the M2 tide off the Atlantic and Pacific coasts of the United States. Journal of Physical Oceanography 12, 8–16.

Blanton, B.O., Werner, F.E., Seim, H.E., Luettich, R.A., Lynch, D.R., Smith, K.W., Voulgaris, G., Bingham, F.M., Way, F., 2004. Barotropic tides in the South Atlantic Bight. Journal of Geophysical Research 109, C12024.

Bruder, B., Bomminayuni, S., Haas, K., Stoesser, T., 2014. Modeling tidal distortion in the Ogeechee Estuary. Ocean Modelling 82, 60–69.

Bunya, S., Dietrich, J.C., Westerink, J.J., Ebersole, B.A., Smith, J.M., Atkinson, J.H., Jensen, R., Resio, D.T., Luettich, R.A., Dawson, C., Cardone, V.J., Cox, A.T., Powell, M.D., Westerink, H.J., Roberts, H.J., 2010. A high-resolution coupled riverine flow, tide, wind, wind wave and storm surge model for southern Louisiana and Mississippi, I: Model development and validation. Monthly Weather Review 138, 345–377.

Clarke, A.J., Battisti, D.S., 1981. The effect of continental shelves on tides. Deep-Sea Research 28A, 665–682.

Dame, R., Alber, M., Allen, D., Mallin, M., Montague, C., Lewitus, A., Chalmers, A., Gardner, R., Bilman, C., Kjerfve, B., Pinckney, J., Smith, N., 2000. Estuaries of the South Atlantic coast of North America: Their geographical signatures. Estuaries 23, 793–819.

de Brye, B., de Brauwere, A., Gourgue, O., Karna, T., Lambrects, J., Comblen, R., Deleersnijder, E., 2010. A finite-element, multi-scale model of the Scheldt tributaries, river, estuary and ROFI. Coastal Engineering 57, 850–863.

Feng, X., Tsimplis, M.N., Woodworth, P.L., 2015. Nodal variations and long-term changes in the main tides on the coasts of China. Journal of Geophysical Research—Oceans 120, 1215–1232.

Flick, R.E., Murray, J.F., Ewing, L.C., 2013. Trends in United States tidal datum statistics and tide range. Journal of Waterway, Port, Coastal and Ocean Engineering 129, 155–164.

Friedrichs, C.T., Aubrey, D.G., 1994. Tidal propagation in strongly convergent channels. Journal of Geophysical Research 99, 3321–3336.

Gesch, D.B., Oimoen, M.J., Evans, G.A., 2014. Accuracy assessment of the U.S. Geological Survey National Elevation Dataset, and comparison with other large-area elevation datasets—SRTM and ASTER. Open-File Report 2014-1008, 10 p.

Giardino, D., Bacopoulos, P., Hagen, S.C., 2011. Tidal spectroscopy of the lower St. Johns River from a high-resolution shallow water hydrodynamic model. International Journal of Ocean and Climate Systems 2, 1–18.

Gonella, J., 1972. A rotary-component method for analyzing meteorological and oceanographic vector time series. Deep-Sea Research 19A, 833–846.

Hagen, S.C., Morris, J.T., Bacopoulos, P., Weishampel, J.F., 2013. Sea-level rise impact on a salt marsh system of the lower St. Johns River. Journal of Waterway, Port, Coastal and Ocean Engineering 139, 118–125.

Hagen, S.C., Westerink, J.J., Kolar, R.L., Horstman, O., 2001. Two-dimensional, unstructured mesh generation for tidal models. International Journal for Numerical Methods in Fluids 35, 669–686.

Hagen, S.C., Zundel, A.K., Kojima, S., 2006. Automatic, unstructured mesh generation for tidal calculations in a large domain. International Journal of Computational Fluid Dynamics 20, 593–608.

Homer, C.G., Dewitz, J.A., Yang, L., Jin, S., Danielson, P., Xian, G., Coulston, J., Herold, N.D., Wickham, J.D., Megown, K., 2015. Completion of the 2011 National Land Cover Database for the conterminous United States: Representing a decade of land cover change information. Photogrammetric Engineering and Remote Sensing 81, 345–354.

Jarrett, J.T., 1976. Tidal prism-inlet area relationships. General Investigation of Tidal Inlets Report 3, U.S. Army Engineer Waterways Experiment Station, Vicksburg, 60 p.

Jones, J.E., Davies, A.M., 2007. A high-resolution finite element model of the M2, M4, M6, S2, N2, K1 and O1 tides off the west coast of Britain. Ocean Modelling 19, 70–100.

Keulegan, G.H., 1967. Tidal flow in entrances: Water-level fluctuations of basins in communication with seas. Technical Bulletin No. 14, Committee on Tidal Hydraulics, U.S. Army Engineer Waterways Experiment Station, Vicksburg, 112 p.

Khangaonkar, T., Long, W., Xu, W., 2017. Assessment of circulation and inter-basin transport in the Salish Sea including Johnstone Strait and Discovery Islands pathways. Ocean Modelling 109, 11–32.

Kolar, R.L., Westerink, J.J., Cantekin, M.E., Blain, C.A., 1994. Aspects of nonlinear simulations using shallow-water models based on the wave continuity equation. Computers and Fluids 23, 523–538.

Kowalik, Z., Polyakov, I., 1998. Tides in the Sea of Okhotsk. Journal of Physical Oceanography 28, 1389–1409.

Le Bars, Y., Vallaeys, V., Deleersnijder, E., Hanert, E., Carrere, L., Channeliere, C., 2016. Unstructured-mesh modeling of the Congo river-to-sea continuum. Ocean Dynamics 66, 589–603.

Le Provost, C., Lyard, F., Molines, J.M., Genco, M.L., Rabilloud, F., 1998. A hydrodynamic ocean tide model improved by assimilating a satellite altimeter-derived data set. Journal of Geophysical Research 103, 5513–5529.

Luettich, R.A., Westerink, J.J., Scheffner, N.W., 1992. ADCIRC: An advanced three-dimensional circulation model for shelves, coasts, and estuaries, I: Theory and methodology of ADCIRC-2DDI and ADCIRC-3DL. Technical Report DRP-92-6, U.S. Army Corps of Engineers, Waterways Experiment Stations, 144p.

Lynch, D.R., Gray, W.G., 1979. A wave equation model for finite element tidal computations. Computers and Fluids 7, 207–228.

Lynch, D., Smith, K., Blanton, B., Luettich, R., Werner, F., 2004. Forecasting the coastal ocean: Resolution, tide and operational data in the South Atlantic Bight. Journal of Atmospheric and Oceanic Technology 21, 1074–1085.

Maas, L.R.M., Doelman, A., 2002. Chaotic tides. Journal of Physical Oceanography 32, 870–890.

Mandelbrot, B., 1967. How long is the coast of Britain? Statistical self-similarity and fractional dimension. Science 156, 636–638.

McKee, K.L., Patrick, W.H., 1988. The relationship of smooth cordgrass (*Spartina alterniflora*) to tidal datums: A review. Estuaries 11, 143–151.

Medeiros, S.C., Hagen, S.C., 2012. Review of wetting and drying algorithms for numerical tidal flow models. Numerical Methods in Fluids 71, 473–487.

NOAA Office for Coastal Management, 2017. General coastline and shoreline mileage of the United States. [Accessed online January 12, 2017: https://coast.noaa.gov/data/docs/states/shorelines.pdf.]

NOAA Tides and Currents, 2015. Center for Operational Oceanographic Products and Services. [Accessed online September 11, 2015: http://tidesandcurrents.noaa.gov/.]

Palma, E.D., Matano, R.P., Piola, A.R., 2004. A numerical study of the Southwestern Atlantic Shelf circulation: Barotropic response to tidal and wind forcing. Journal of Geophysical Research Oceans 109, C08014.

Parker, B.B., 1991. The relative importance of the various nonlinear mechanisms in a wide range of tidal interactions (review). *In:* Parker, B.B. (ed.), *Tidal Hydrodynamics*, New York: John Wiley and Sons, pp. 79–108.

Parker, B.B., Hess, K., Milbert, D., Gill, S., 2003. A national vertical datum transformation tool. Sea Technology 44, 10–15.

Parkman, A., 1983. History of the waterways of the Atlantic coast of the United States. Navigation History NWS-83-10, National Waterways Study, U.S. Army Engineer Water Resources Support Center, Institute for Water Resources, Virginia, 147 p.

Parrish, D.M., Hagen, S.C., 2009. Incorporating spatially variable bottom stress and Coriolis force into 2D, a posteriori, unstructured mesh generation for shallow water models. International Journal for Numerical Methods in Fluids 60, 237–261.

Pelling, H.E., Mattias Green, J.A., Ward, S.L., 2013. Modelling tides and sea-level rise: To flood or not to flood. Ocean Modelling 63, 21–29.

Pugh, D., Woodworth, P., 2014. Sea-level science: Understanding tides, surges, tsunamis and mean sea-level changes. Cambridge University Press, 395 p.

Redfield, A., 1958. The influence of the continental shelf on the tides of the Atlantic coast of the United States. Journal of Marine Research 17, 432–448.

Robins, P.E., Skov, M.W., Lewis, M.J., Gimenez, L., Davies, A.G., Malham, S.K., Neill, S.P., McDonald, J.E., Whitton, T.A., Jackson, S.E., 2016. Impact of climate change on UK estuaries: A review of past trends and potential projections. Estuarine, Coastal and Shelf Science 169, 119–135.

Savenije, H.H.G., 2012. Salinity and tides in alluvial estuaries, 2$^{nd}$ revision. Delft University of Technology, The Netherlands, 173p.

Schureman, P., 1941. Manual of harmonic analysis and prediction of tides. Special Publication No. 98, Coast and Geodetic Survey, U.S. Department of Commerce, Washington, DC, 336 p.

Seim, H., Blanton, J., Elston, S., 2006. Tidal circulation and energy dissipation in a shallow, sinuous estuary. Ocean Dynamics 56, 360–375.

Seim, H.E., Fletcher, M., Mooers, C.N.K., Nelson, J.R., Weisberg, R.H., 2009. Towards a regional coastal ocean observing system: An initial design for the Southeast Coastal Ocean Observing Regional Association. Journal of Marine Systems 77, 261–277.

Shearman, R.K., Lentz, S.J., 2004. Observations of tidal variability on the New England shelf. Journal of Geophysical Research Oceans 109, C06010.

Shepard, A.N., 2015. South Atlantic Bight: Bitten by worsening problems. National Oceanic and Atmospheric Administration. [Accessed online September 11, 2015: http://oceanexplorer.noaa.gov/explorations/islands01/background/bight/bight.html.]

Smith, N.P., 2001. Seasonal-scale transport patterns in a multi-inlet coastal lagoon. Estuarine, Coastal and Shelf Science 52, 15–28.

Tamura, H., Bacopoulos, P., Wang, D., Hagen, S.C., Kubatko, E.J., 2014. State estimation of hydrodynamics in the lower St. Johns River using ensemble Kalman filter. Advances in Water Resources 63, 45–56.

Van, C.P., de Brye, B., Deleersnijder, E., Hoitink, A.J.F., Sassi, M., Spinewine, B., Hidayat, H., Soares-Frazao, S., 2016. Simulations of the flow in the Mahakam river-lake-delta system, Indonesia. Environmental Fluid Mechanics 16, 603–633.

Vertical Datum Transformation, 2016. Frequently asked questions: Why doesn’t VDatum provide tidal datums inland? [Accessed online February 5, 2016: https://vdatum.noaa.gov/docs/faqs.html.]

Westerink, J.J., Luettich, R.A., Feyen, J.C., Atkinson, J.H., Dawson, C.N., Roberts, H.J., Powell, M.D., Dunion, J.P., Kubatko, E.J., Pourtaheri, H., 2008. A basin to channel scale unstructured grid hurricane storm surge model applied to southern Louisiana. Monthly Weather Review 136, 833–864.

Yang, W., Myers, E.P., Jeong, I., White, S.A., 2012. VDatum for coastal waters from the Florida Shelf to the South Atlantic Bight: Tidal datums, marine grids and the sea surface topography. NOAA Technical Memorandum NOS CS 27, Washington, DC, 107 p.

Fig. 1. The South Atlantic Bight is open to the western North Atlantic Ocean and bounded by the Florida, Georgia and Carolina coastlines. The inset zooms in on the northeast Florida, Georgia and southeast South Carolina coastline. The black-filled zones along the landward periphery of the in-bank mesh triangulation that is displayed are the intertidal zones.

Fig. 2. Finite element mesh for the South Atlantic Bight and its estuaries and intertidal zones. Insets show the definition of the St. Johns River at the estuary scale and the representation of the tidal creek-salt marsh system of the Timucuan Preserve. The 16 stations are those located in tidal creeks.

Fig. 3a. Locator map of the 142 gaging stations in the South Atlantic Bight from where tidal data were gathered. The yellow "+" symbols denote the stations located in partition 1. The shelf gaging stations where velocity data are compared with model results are labeled as GR, R2, R5 and R6.

Fig. 3b. Modeled vs. observed tidal datums (MLW and MHW) are plotted in scatter format for the estuary stations of the South Atlantic Bight (129 total), shown with best-fit lines, equations of best-fit lines and $R^2$ values. The top panel displays the model results for the MARSH mesh, and the bottom panel is for the AIW mesh. The eight (partition 1) stations are denoted by background (white-filled) circles.

Fig. 4a. Spatial fields of $M_2$ velocity amplitude ratios based on the AIW vs. COAST model results. Five cross-shelf transects were drawn from the coastline to the shelf break for partition 1 of the South Atlantic Bight.

Fig. 4b. Same as Figure 4a, but zoomed in on the Altamaha and St. Mary's Rivers.

Fig. 5. Tidal amplification according to simulated $M_2$ tidal velocities and continental margin theory (scale factor—$v$) as a function of shelf width and effective shelf width (AIW vs. COAST). The five panels correspond to the five transects of the continental shelf for partition 1 of the South Atlantic Bight. The horizontal lines represent the transect-averaged (| |) values.

Fig. 6a. Spatial fields of $M_2$ velocity amplitude ratios based on the MARSH vs. AIW model results.

Fig. 6b. Same as Figure 6a, but zoomed in on the Altamaha and St. Mary's Rivers.

Fig. 7. Spatial fields of energy dissipation for a characteristic spring $M_2$ tidal cycle in the South Atlantic Bight based on the MARSH model results. The river/channel banks are shown for reference as the delineation between the fully wetted zones and intertidal zones. The regional energy dissipation due to bottom stress ($P_{bot}$) within the window extents of the graphics is labeled on each panel along with percent of the regional energy dissipation associated with the intertidal zones (Marsh).

Fig. A1. Panels showing the distances, inlets, estuaries/rivers and marshes/lagoons of the South Atlantic Bight. Partition 1 includes the 27 inlets from Winyah Bay, South Carolina to the Florida/Georgia border (grey shaded). Partition 2 includes the 37 inlets for the coastline of the southern portion of North Carolina, the northern portion of South Carolina and Florida's east coast.

Fig. B1. Bar charts of tidal datums (MLW and MHW) for the estuary stations (129 total) of the South Atlantic Bight, where the model results shown are those from the best-performing mesh (MARSH). The stars (8 total) denote the stations located in partition 1.

Fig. B2. There is a total of 16 gaging stations that contain tidal data for tidal creeks in the South Atlantic Bight estuaries/marshes, which are listed from north to south, annotated with the location type and plotted as distance from nearest inlet mouth. A 14.77-day synthesis of the tidal signal is shown as data versus model (best-performing results: MARSH) for each of the 16 tidal-creek gaging stations, where the bottom panel shows the corresponding root mean square errors of the data-model fits for MARSH and AIW.

Fig. B3a. Parametric tide plots in polar space of data versus model (best-performing results: MARSH) for spring (day 0–1) and neap (day 7–8) tidal cycles with corresponding charts of lower low water (LLW), low water (LW), high water (HW) and higher high water (HHW) for Sisters Creek—Intracoastal Waterway.

Fig. B3b. Same as Figure B3a, but for Clapboard Creek—St. Johns River.

**Figure 1**

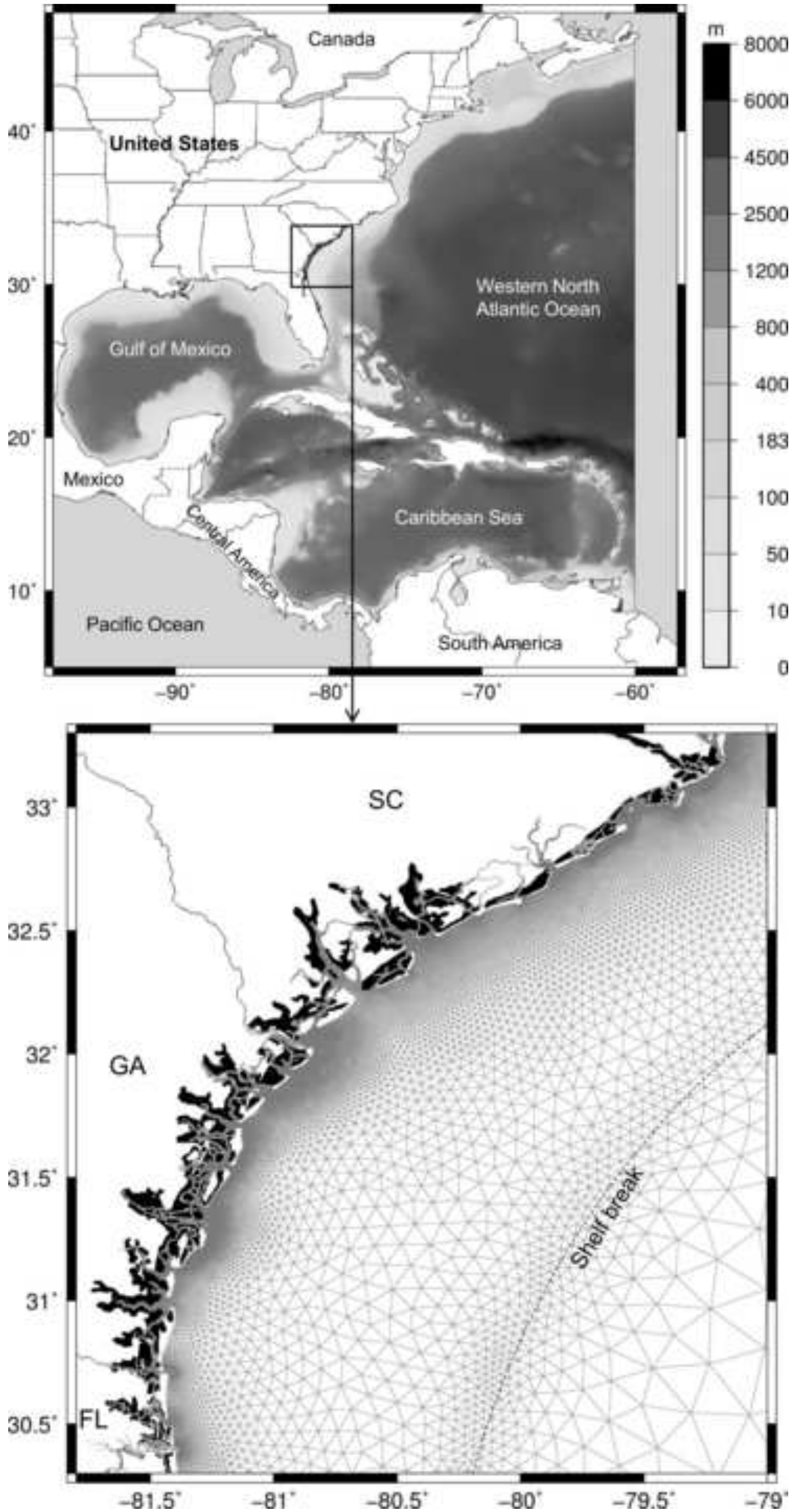

Canada
United States
Gulf of Mexico
Western North Atlantic Ocean
Mexico
Central America
Caribbean Sea
Pacific Ocean
South America
40°
30°
20°
10°
-90°
-80°
-70°
-60°
m
8000
6000
4500
2500
1200
800
400
183
100
50
10
0
SC
GA
FL
Shelf break
33°
32.5°
32°
31.5°
31°
30.5°
-81.5°
-81°
-80.5°
-80°
-79.5°
-79°

**Figure 2**

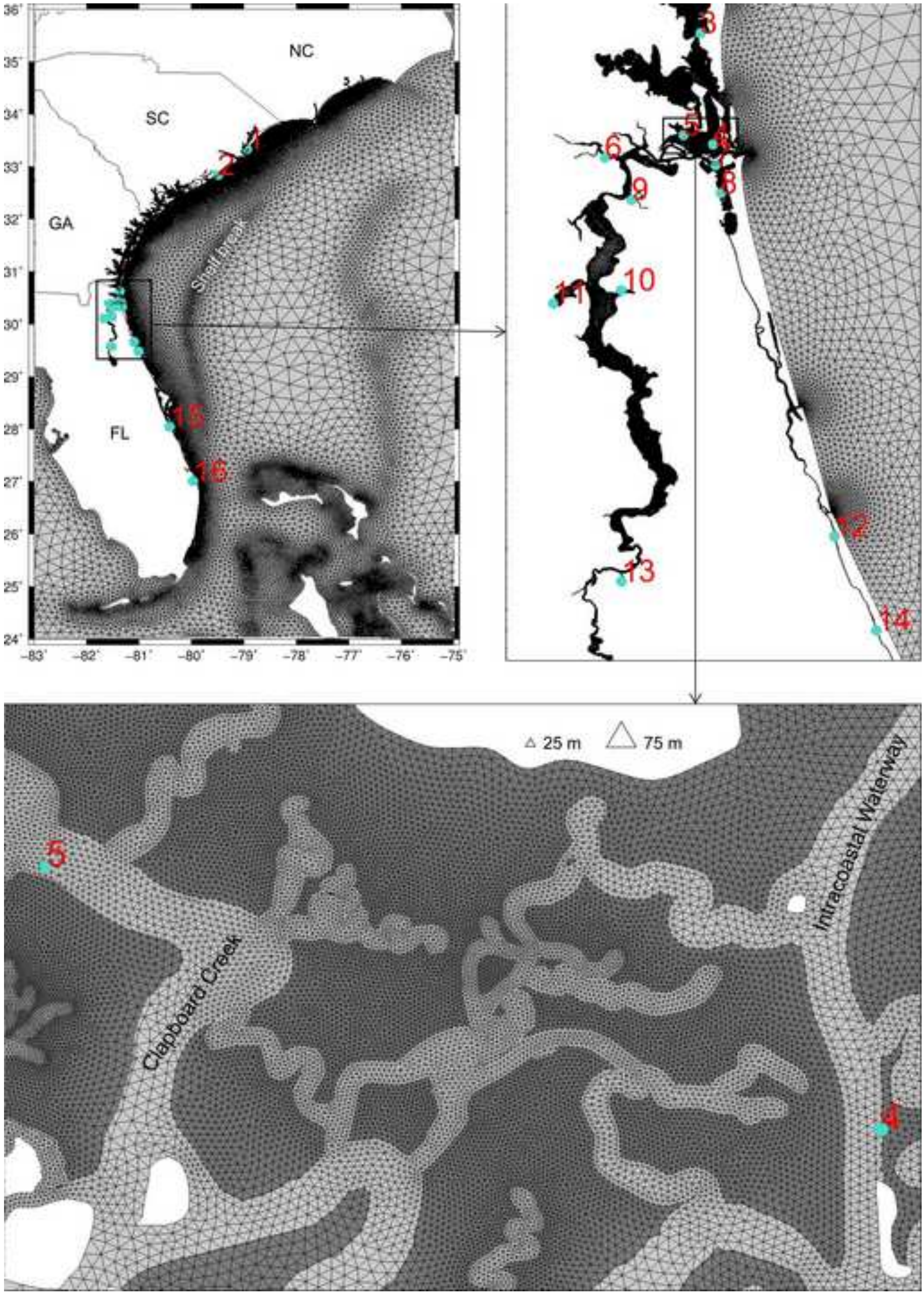
NC
SC
GA
FL
Shelf break
1
2
15
16
36°
35°
34°
33°
32°
31°
30°
29°
28°
27°
26°
25°
24°
-83°
-82°
-81°
-80°
-79°
-78°
-77°
-76°
-75°
3
5
4
6
8
9
10
11
12
13
14
25 m
75 m
Intracoastal Waterway
Clapboard Creek
5
4

**Figure 3a**

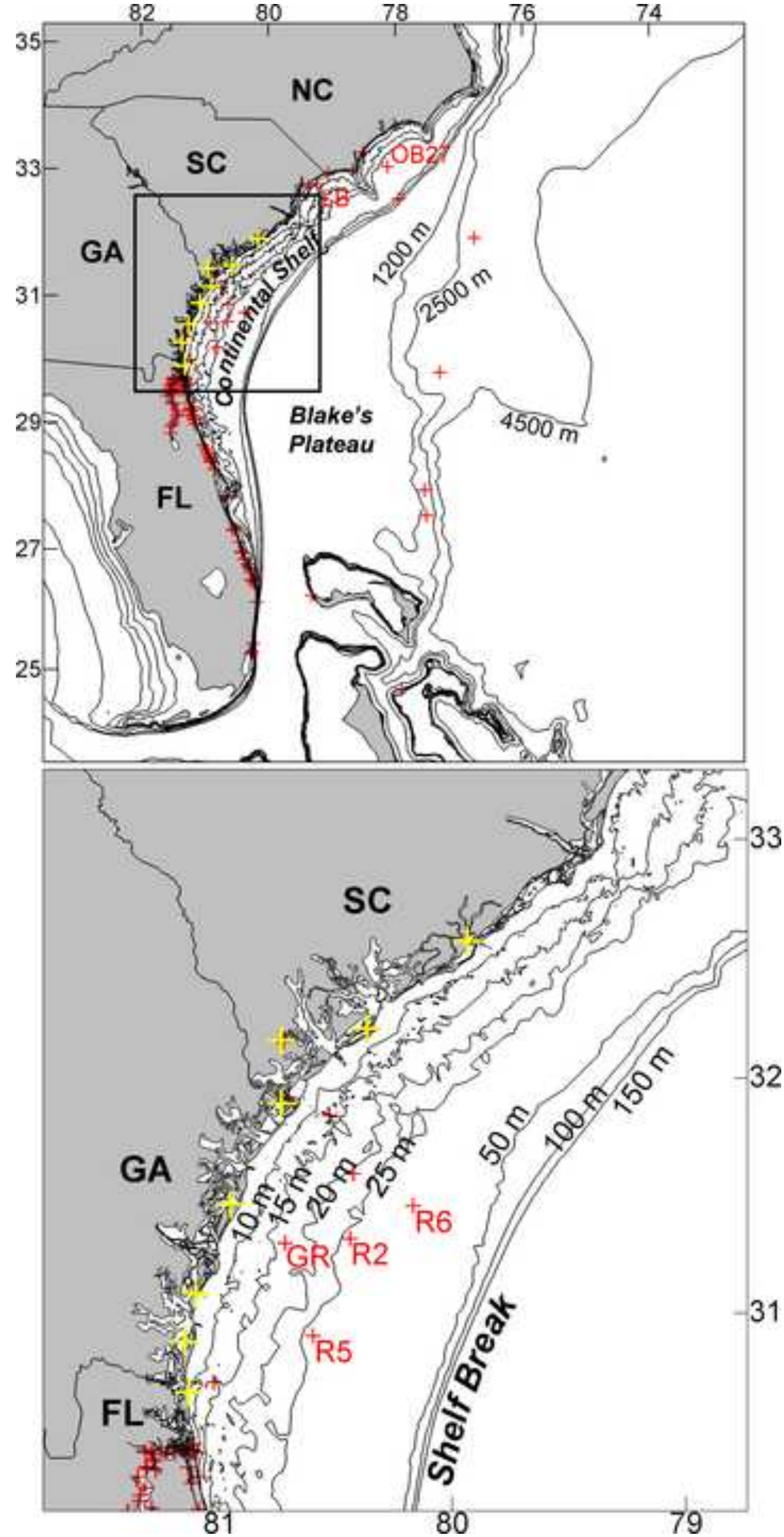

82
80
78
76
74
35
33
31
29
27
25
NC
SC
GA
FL
OB27
EB
Continental Shelf
1200 m
2500 m
4500 m
Blake's Plateau
SC
GA
FL
33
32
31
81
80
79
10 m
15 m
20 m
25 m
50 m
100 m
150 m
R6
GR
R2
R5
Shelf Break

**Figure 3b**

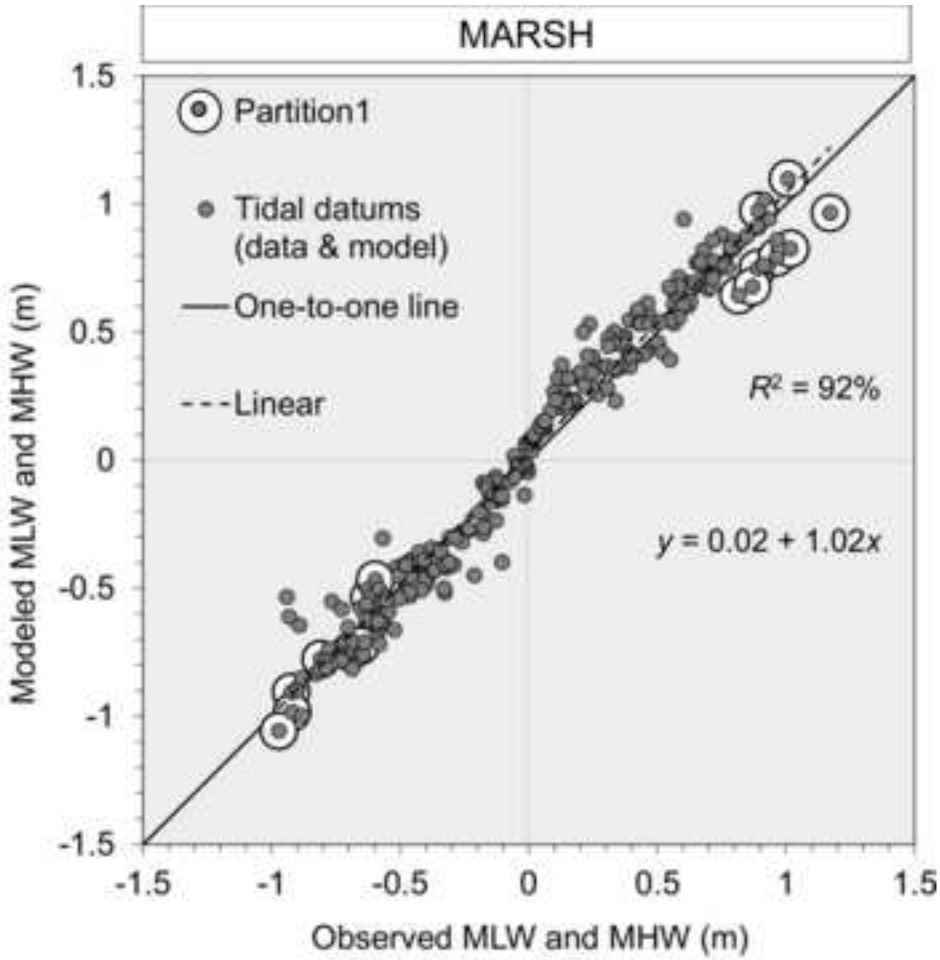

MARSH
Partition1
Tidal datums
(data & model)
One-to-one line
Linear
R2 = 92%
y = 0.02 + 1.02x
Modeled MLW and MHW (m)
Observed MLW and MHW (m)
-1.5
-1
-0.5
0
0.5
1
1.5


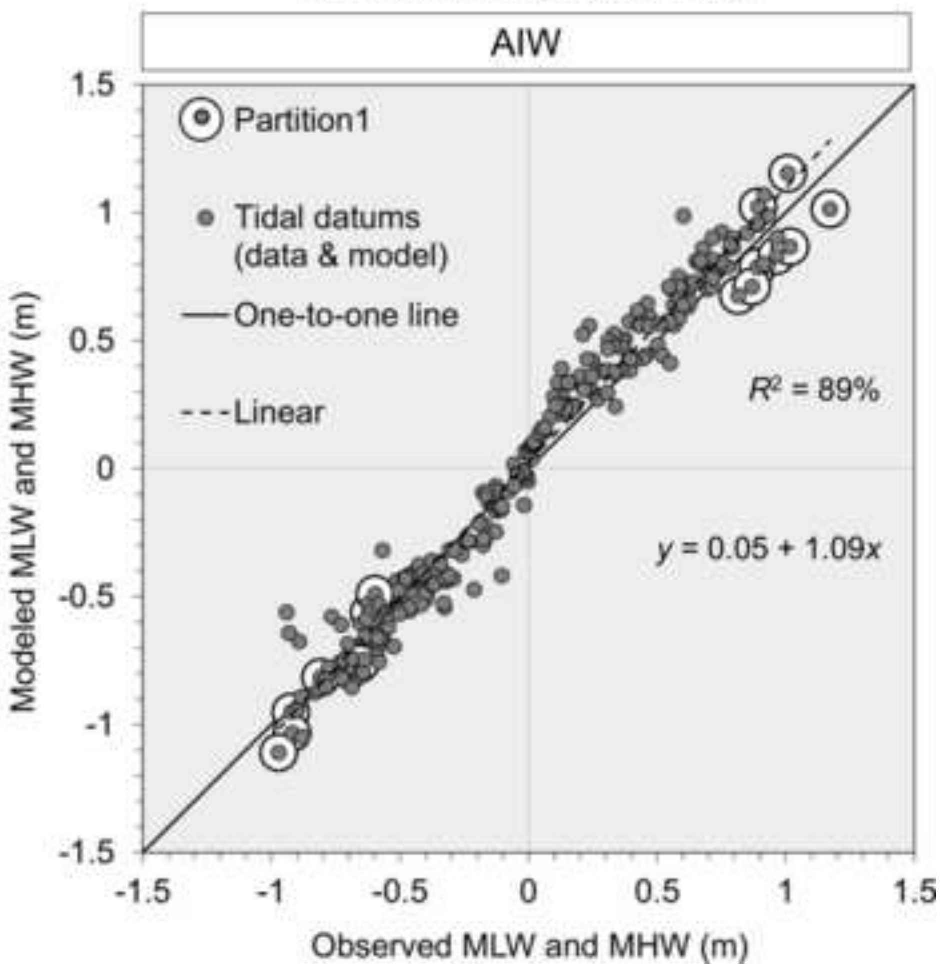

AIW
Partition1
Tidal datums
(data & model)
One-to-one line
Linear
R2 = 89%
y = 0.05 + 1.09x
Modeled MLW and MHW (m)
Observed MLW and MHW (m)
-1.5
-1
-0.5
0
0.5
1
1.5

**Figure 4a**

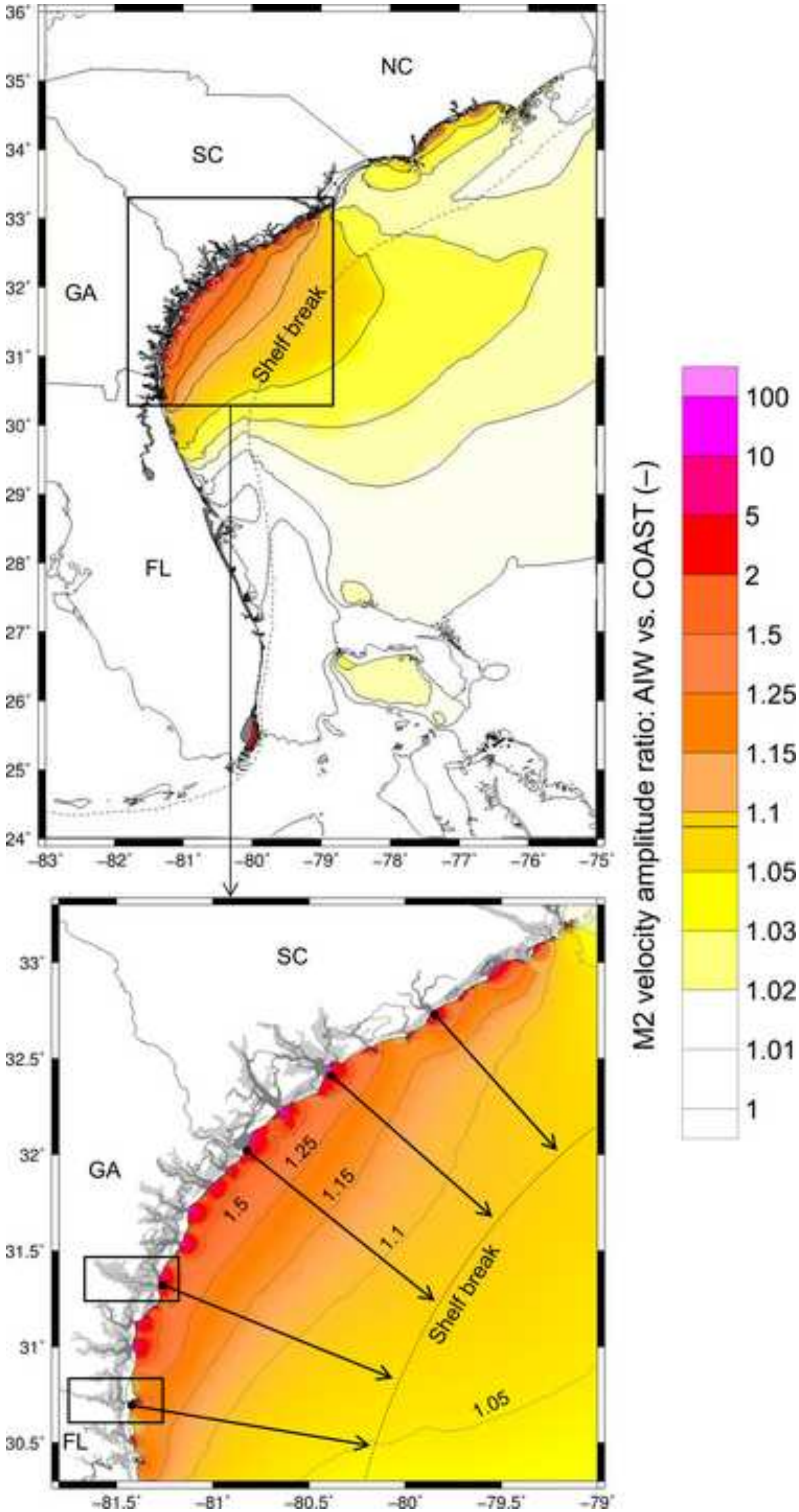

NC
SC
GA
FL
Shelf break
36°
35°
34°
33°
32°
31°
30°
29°
28°
27°
26°
25°
24°
-83°
-82°
-81°
-80°
-79°
-78°
-77°
-76°
-75°
1.25
1.15
1.5
1.1
1.05
33°
32.5°
32°
31.5°
31°
30.5°
-81.5°
-81°
-80.5°
-80°
-79.5°
-79°
M2 velocity amplitude ratio: AIW vs. COAST (–)
100
10
5
2
1.5
1.25
1.15
1.1
1.05
1.03
1.02
1.01
1

Figure 4b

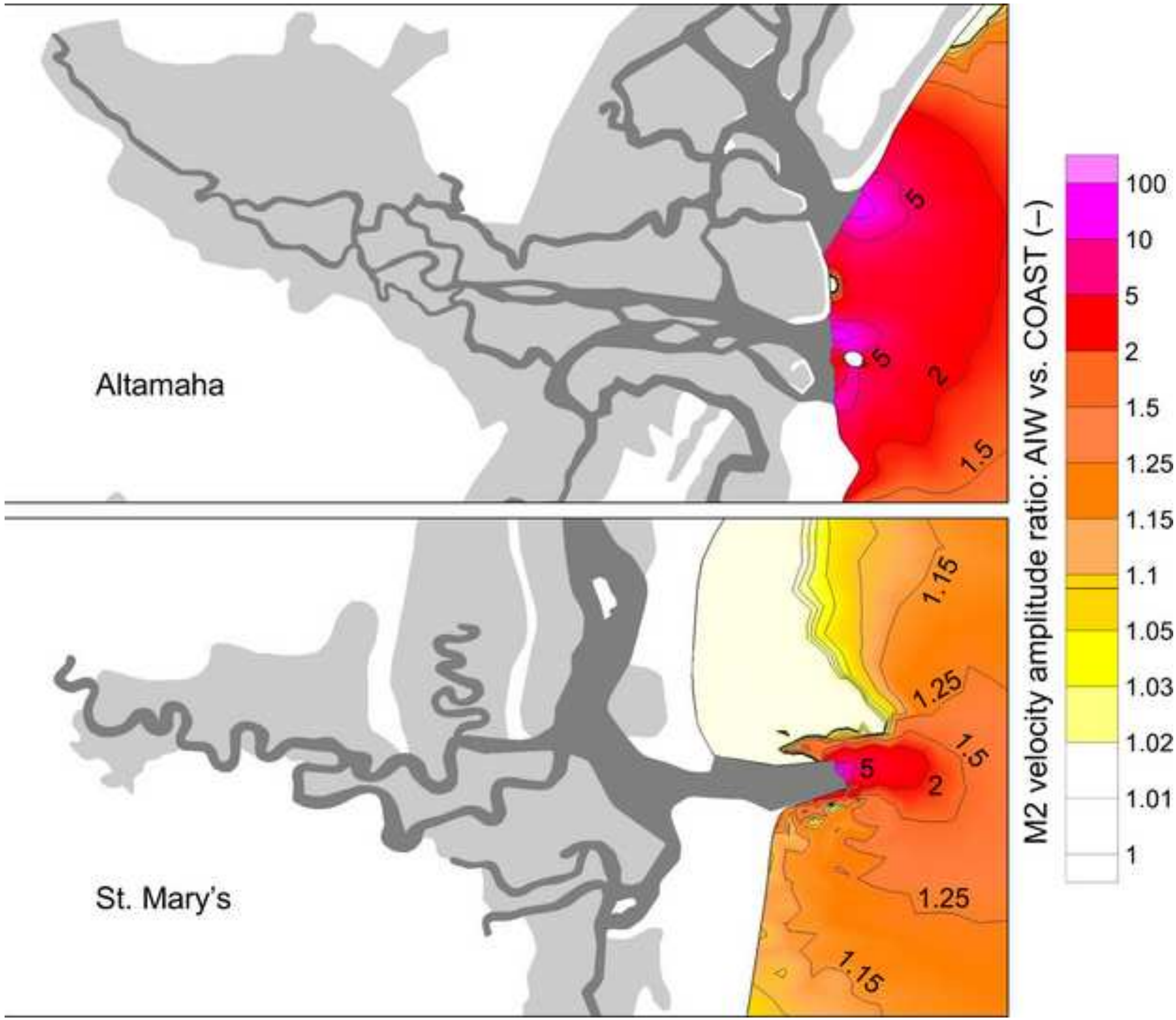

Altamaha
5
5
2
1.5
St. Mary's
1.15
1.25
1.5
5
2
1.25
1.15
100
10
5
2
1.5
1.25
1.15
1.1
1.05
1.03
1.02
1.01
1
M2 velocity amplitude ratio: AIW vs. COAST (–)

**Figure 5**

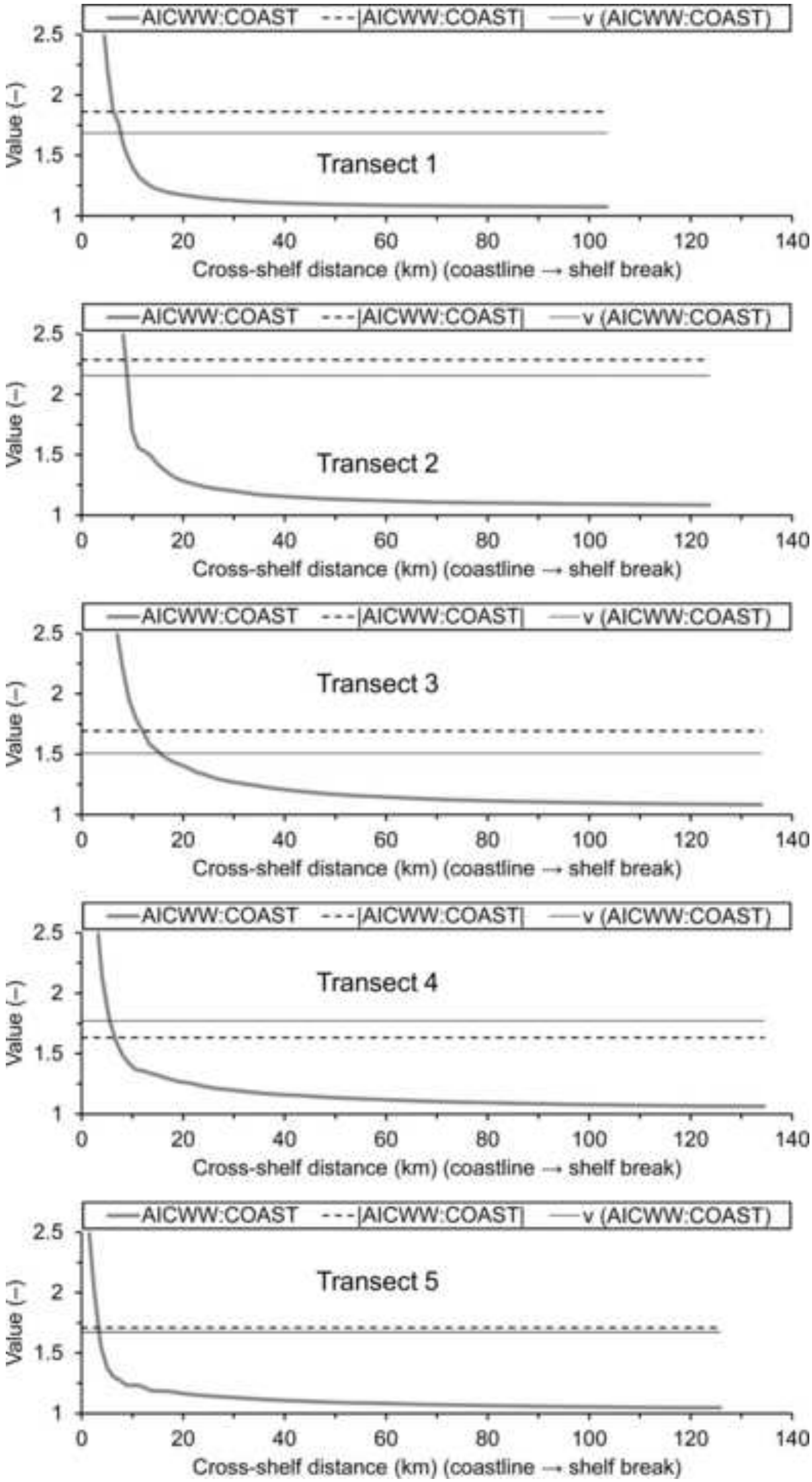
AICWW:COAST
|AICWW:COAST|
v (AICWW:COAST)
Transect 1
Transect 2
Transect 3
Transect 4
Transect 5
Value (–)
Cross-shelf distance (km) (coastline → shelf break)
0
20
40
60
80
100
120
140
1
1.5
2
2.5

Figure 6a

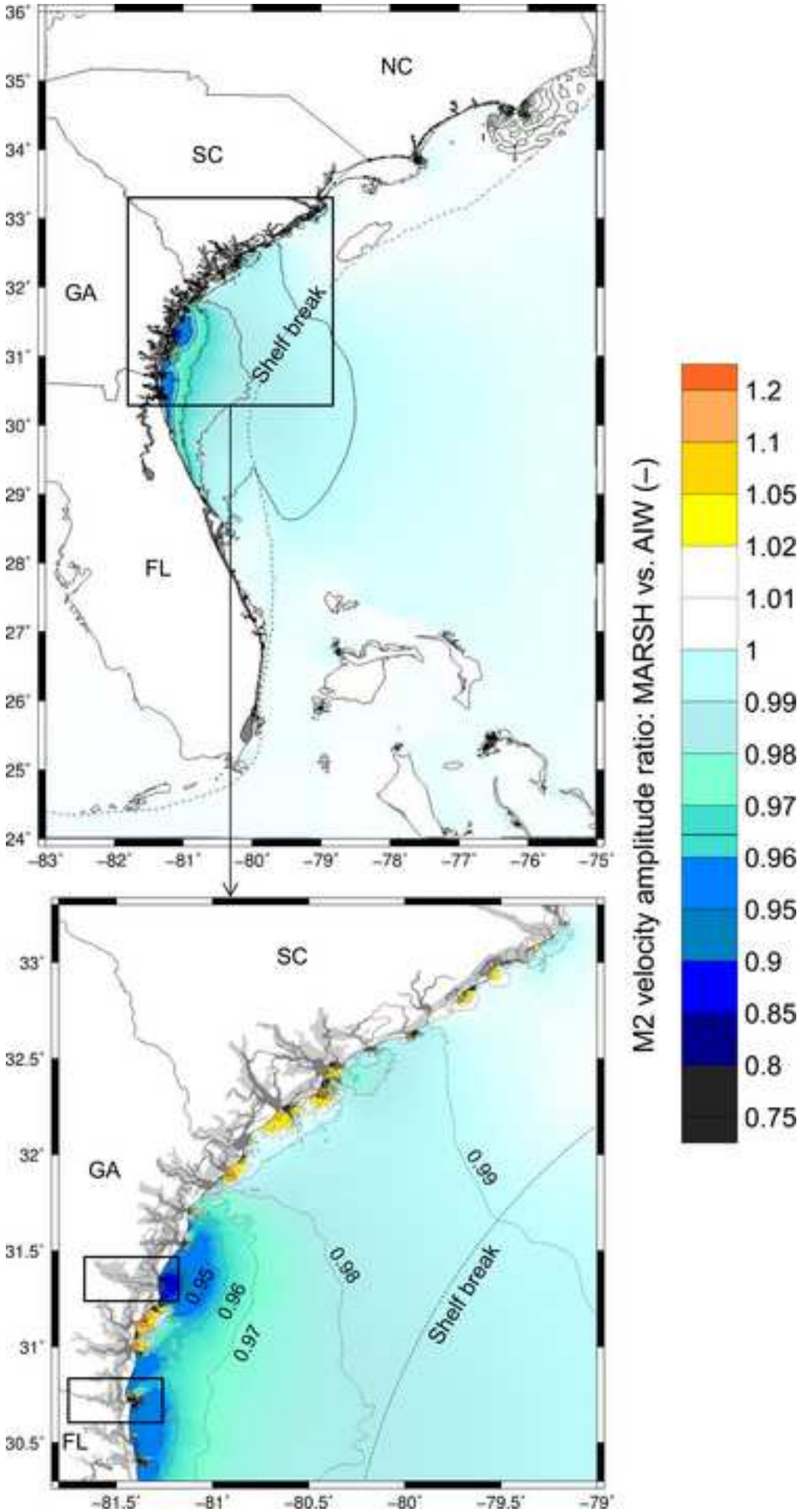

NC
SC
GA
FL
Shelf break
36°
35°
34°
33°
32°
31°
30°
29°
28°
27°
26°
25°
24°
-83°
-82°
-81°
-80°
-79°
-78°
-77°
-76°
-75°
SC
GA
FL
0.95
0.96
0.97
0.98
0.99
Shelf break
33°
32.5°
32°
31.5°
31°
30.5°
-81.5°
-81°
-80.5°
-80°
-79.5°
-79°
M2 velocity amplitude ratio: MARSH vs. AIW (–)
1.2
1.1
1.05
1.02
1.01
1
0.99
0.98
0.97
0.96
0.95
0.9
0.85
0.8
0.75

Figure 6b

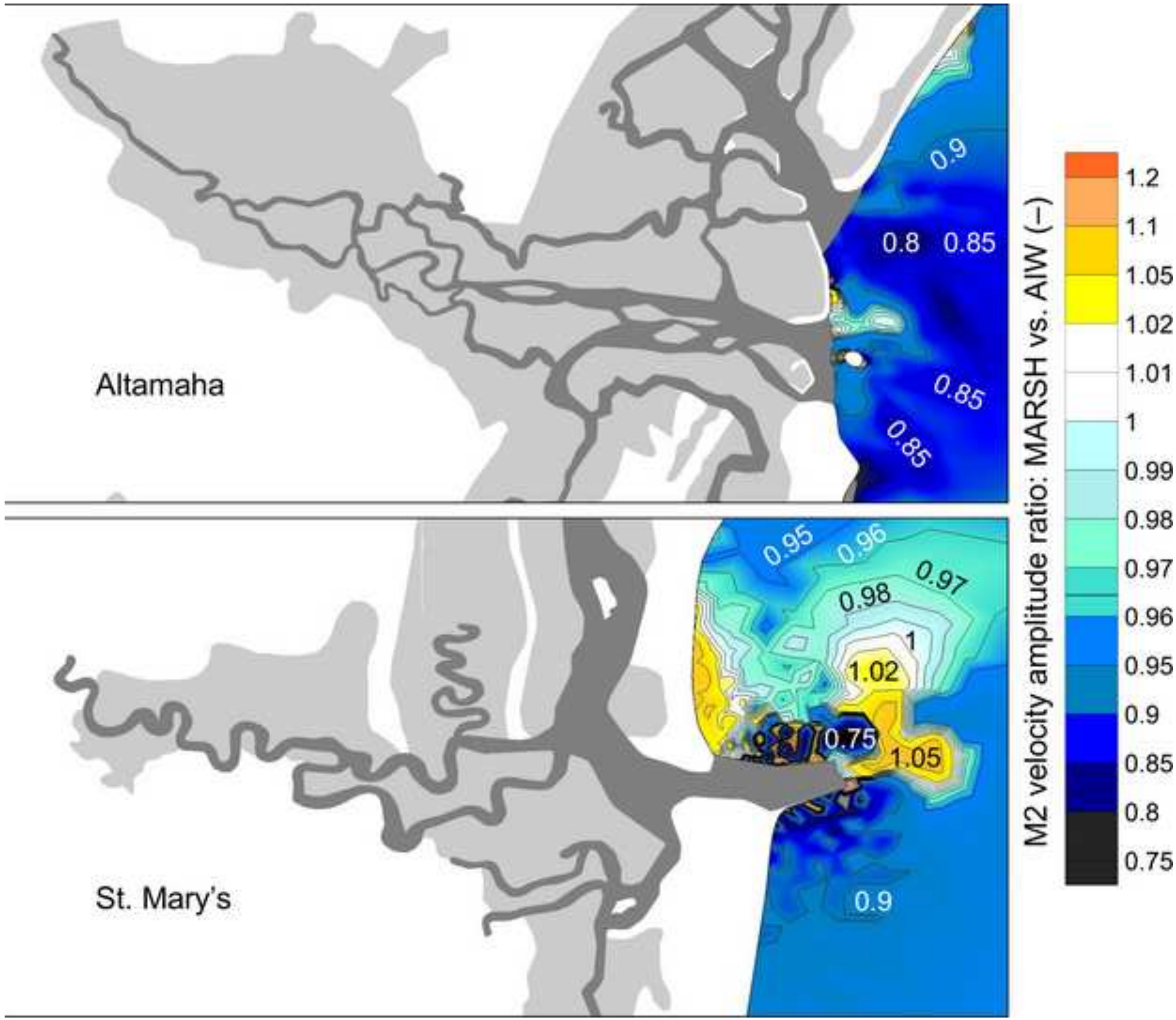
Altamaha
0.9
0.8
0.85
0.85
0.85
St. Mary's
0.95
0.96
0.97
0.98
1
1.02
0.75
1.05
0.9
M2 velocity amplitude ratio: MARSH vs. AIW (–)
1.2
1.1
1.05
1.02
1.01
1
0.99
0.98
0.97
0.96
0.95
0.9
0.85
0.8
0.75

**Figure 7**

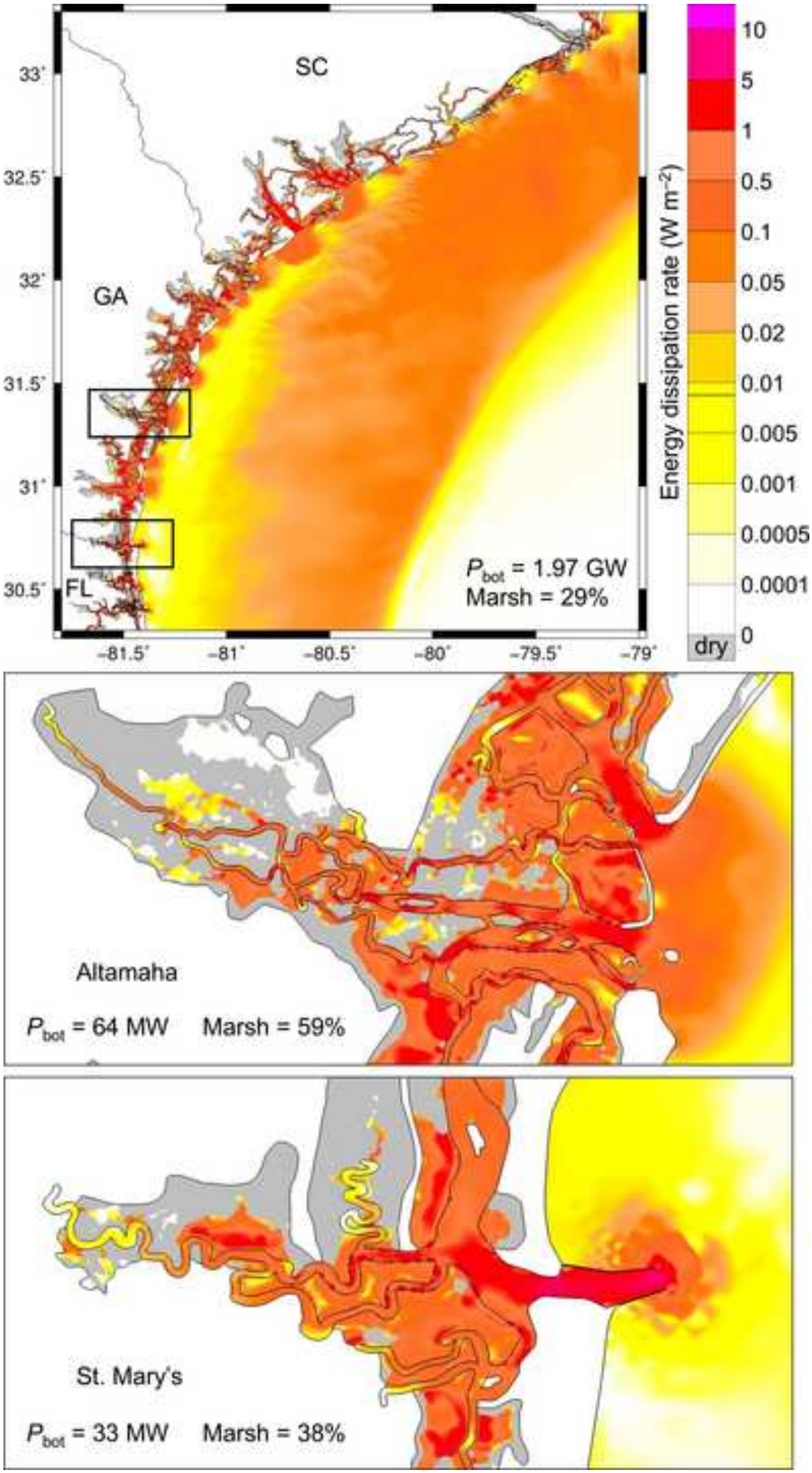
SC
GA
FL
33°
32.5°
32°
31.5°
31°
30.5°
-81.5°
-81°
-80.5°
-80°
-79.5°
-79°
$P_{bot}$ = 1.97 GW
Marsh = 29%
10
5
1
0.5
0.1
0.05
0.02
0.01
0.005
0.001
0.0005
0.0001
0
dry
Energy dissipation rate (W m$^{-2}$)
Altamaha
$P_{bot}$ = 64 MW
Marsh = 59%
St. Mary's
$P_{bot}$ = 33 MW
Marsh = 38%

**Figure A1**

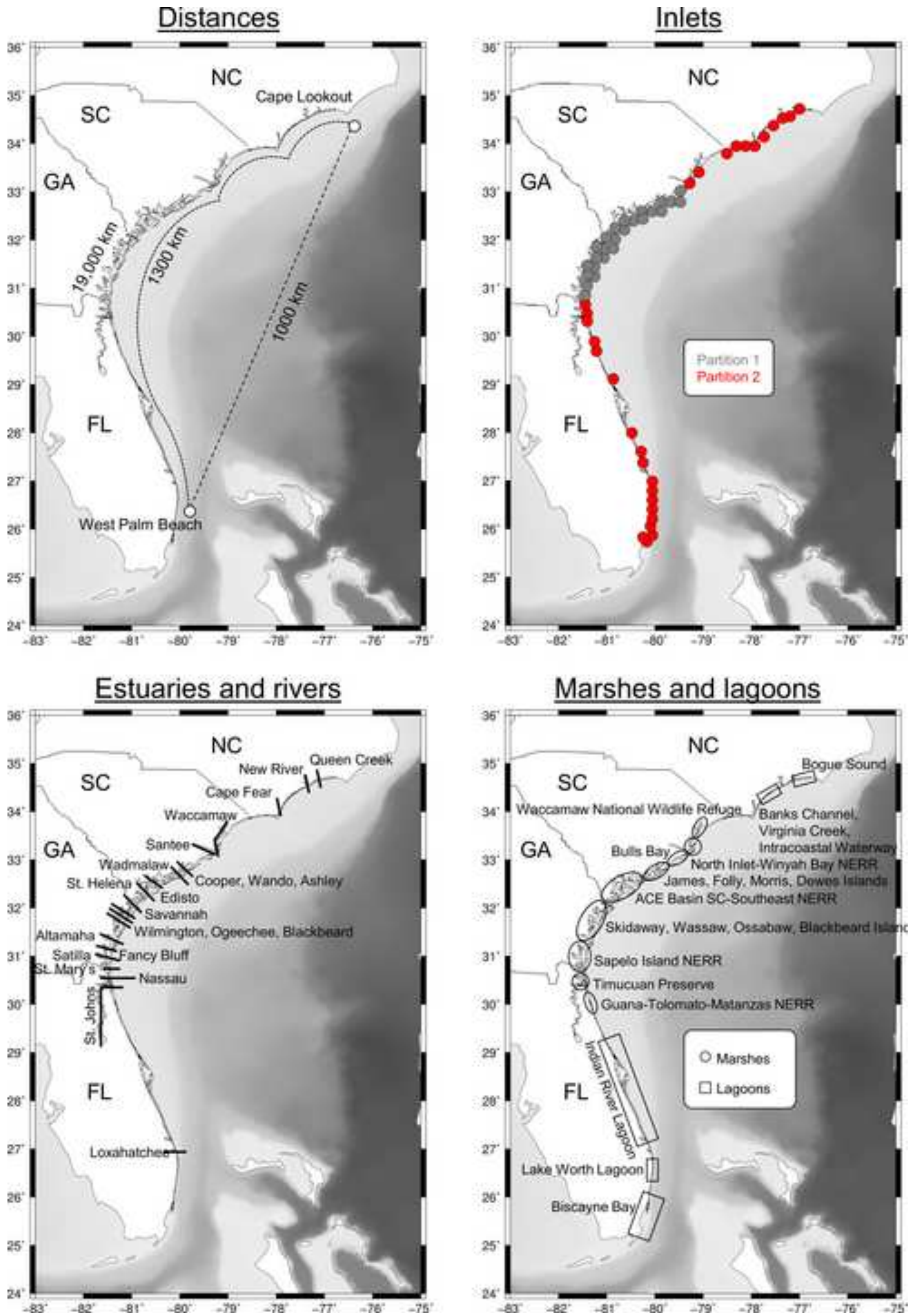
Distances
NC
SC
GA
FL
Cape Lookout
19,000 km
1300 km
1000 km
West Palm Beach
Inlets
NC
SC
GA
FL
Partition 1
Partition 2
Estuaries and rivers
NC
SC
GA
FL
Queen Creek
New River
Cape Fear
Waccamaw
Santee
Wadmalaw
St. Helena
Cooper, Wando, Ashley
Edisto
Savannah
Wilmington, Ogeechee, Blackbeard
Altamaha
Satilla
Fancy Bluff
St. Mary's
Nassau
St. Johns
Loxahatchee
Marshes and lagoons
NC
SC
GA
FL
Bogue Sound
Waccamaw National Wildlife Refuge
Banks Channel,
Virginia Creek,
Intracoastal Waterway
Bulls Bay
North Inlet-Winyah Bay NERR
James, Folly, Morris, Dewes Islands
ACE Basin SC-Southeast NERR
Skidaway, Wassaw, Ossabaw, Blackbeard Island
Sapelo Island NERR
Timucuan Preserve
Guana-Tolomato-Matanzas NERR
Indian River Lagoon
Marshes
Lagoons
Lake Worth Lagoon
Biscayne Bay

**Figure A1 (greyscale)**

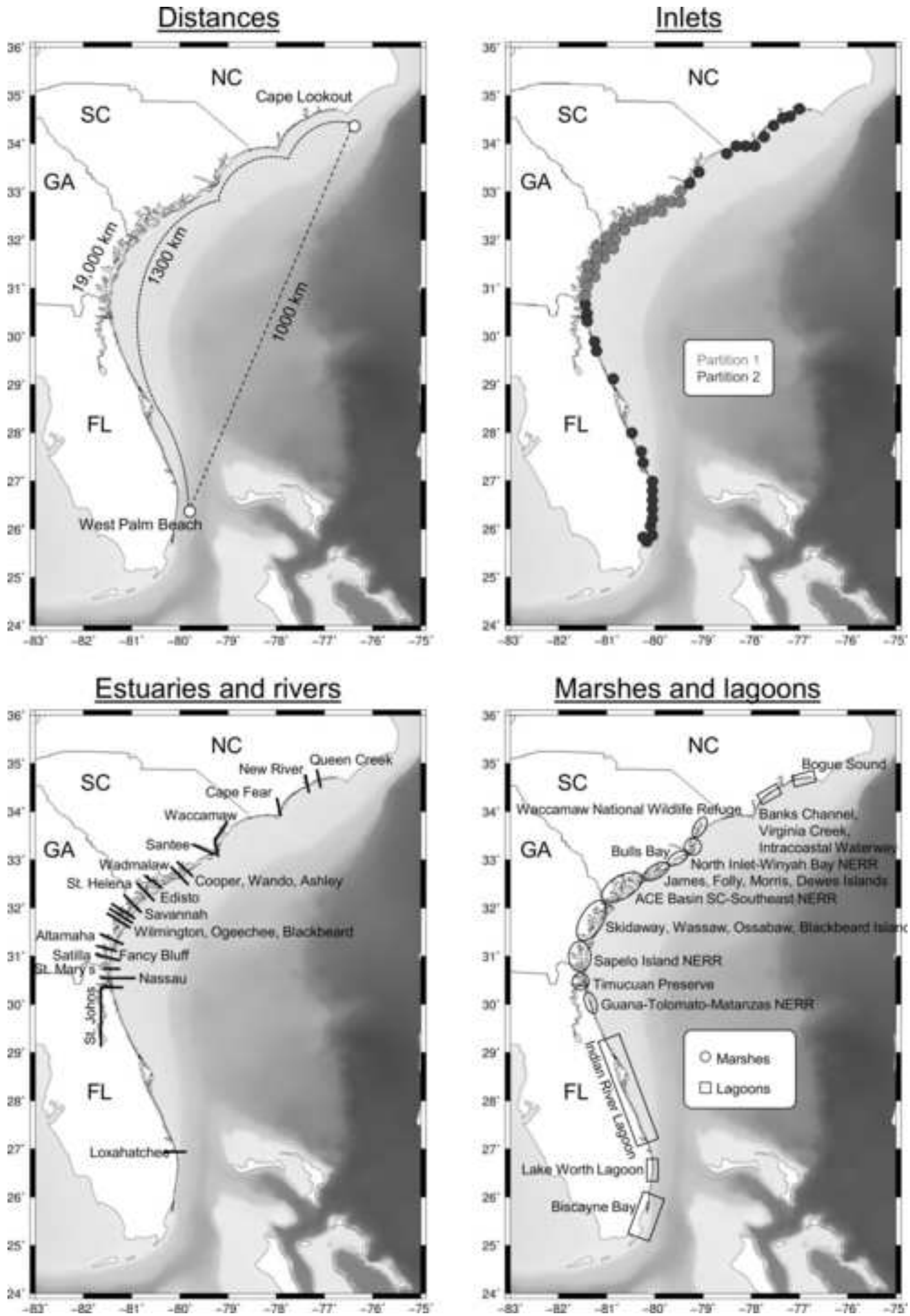

**Figure B1**

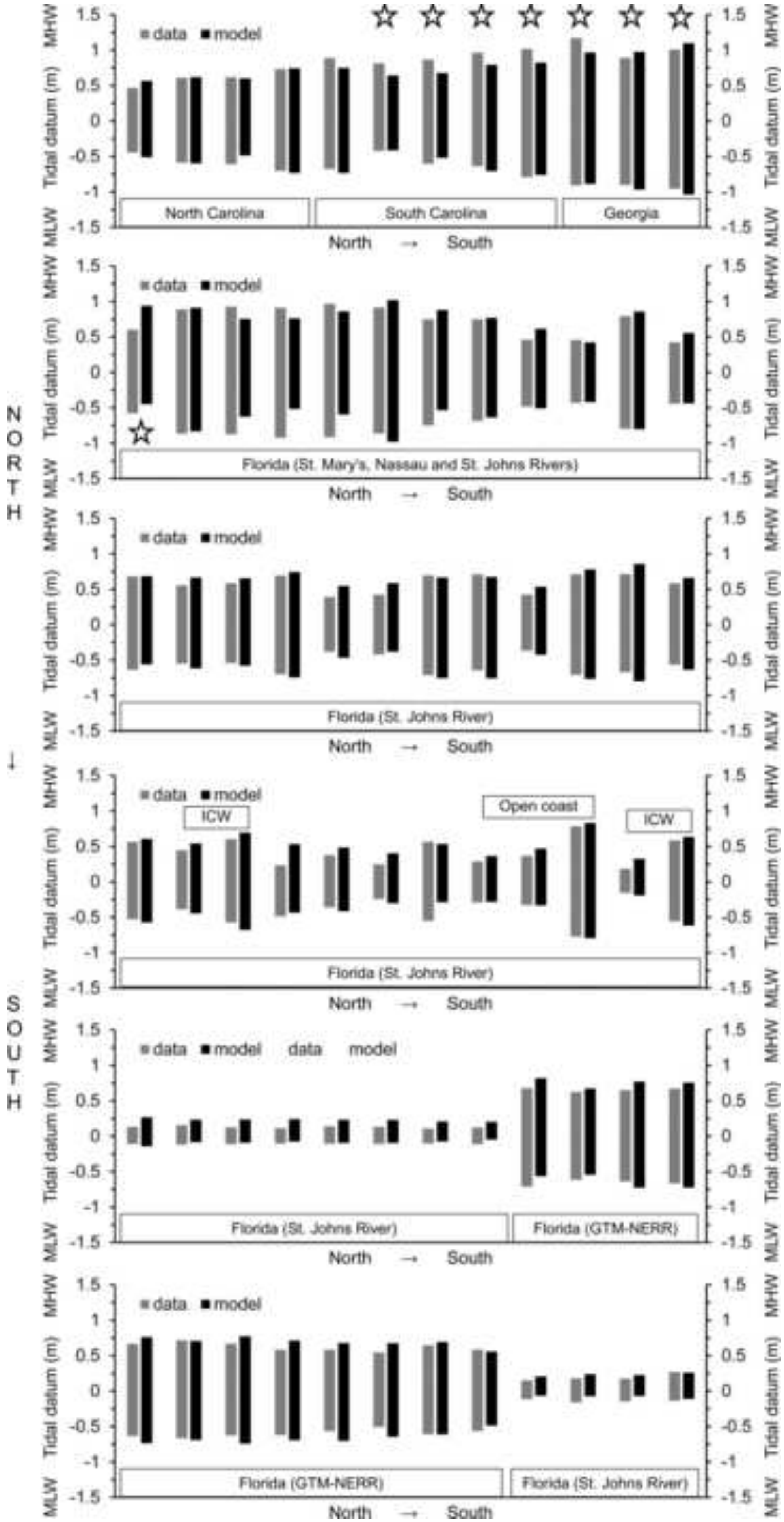
data
model
Tidal datum (m)
MHW
MLW
North Carolina
South Carolina
Georgia
Florida (St. Mary's, Nassau and St. Johns Rivers)
Florida (St. Johns River)
ICW
Open coast
Florida (GTM-NERR)
North → South
NORTH
SOUTH

**Figure B1 (continued)**

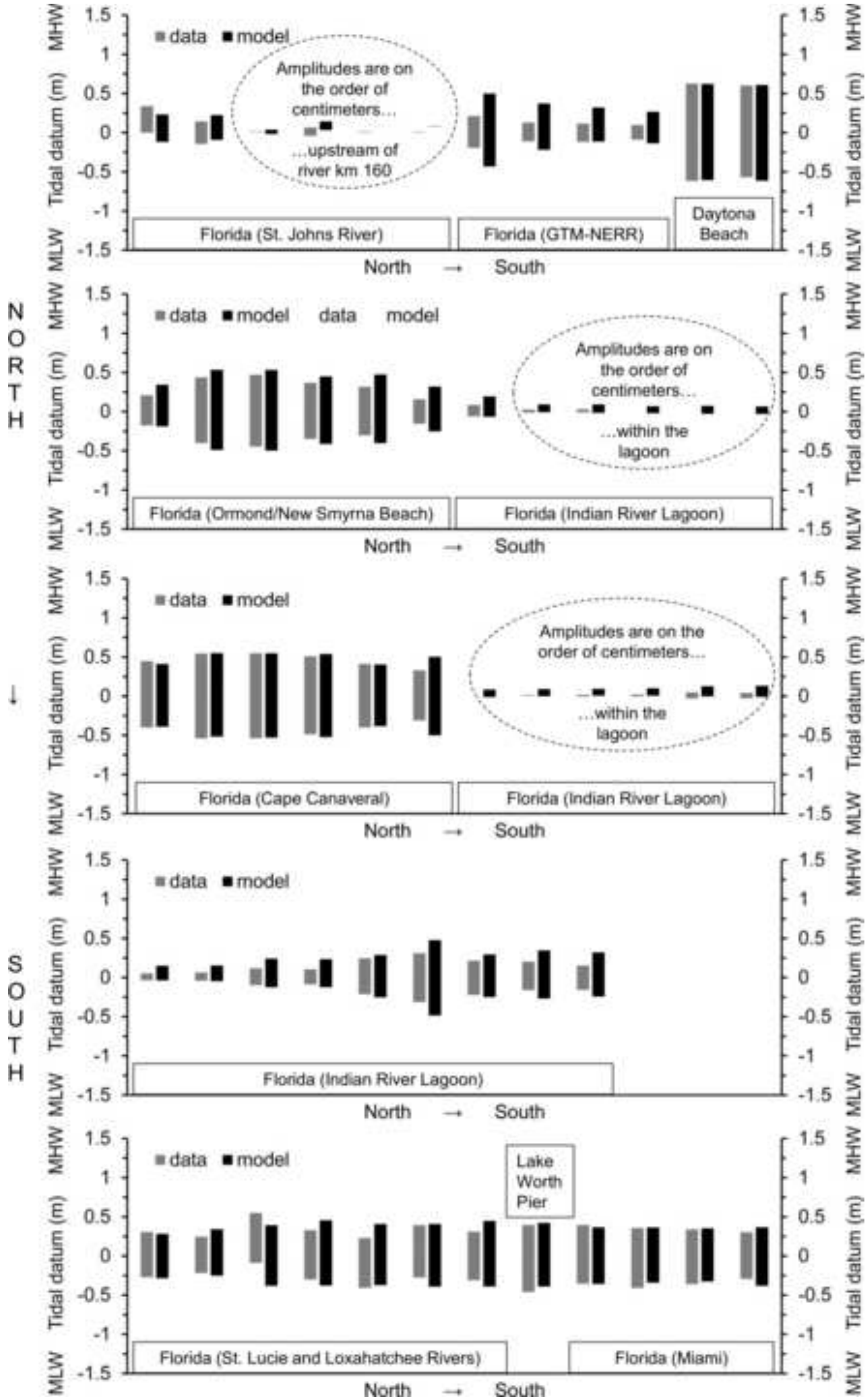

Figure B2

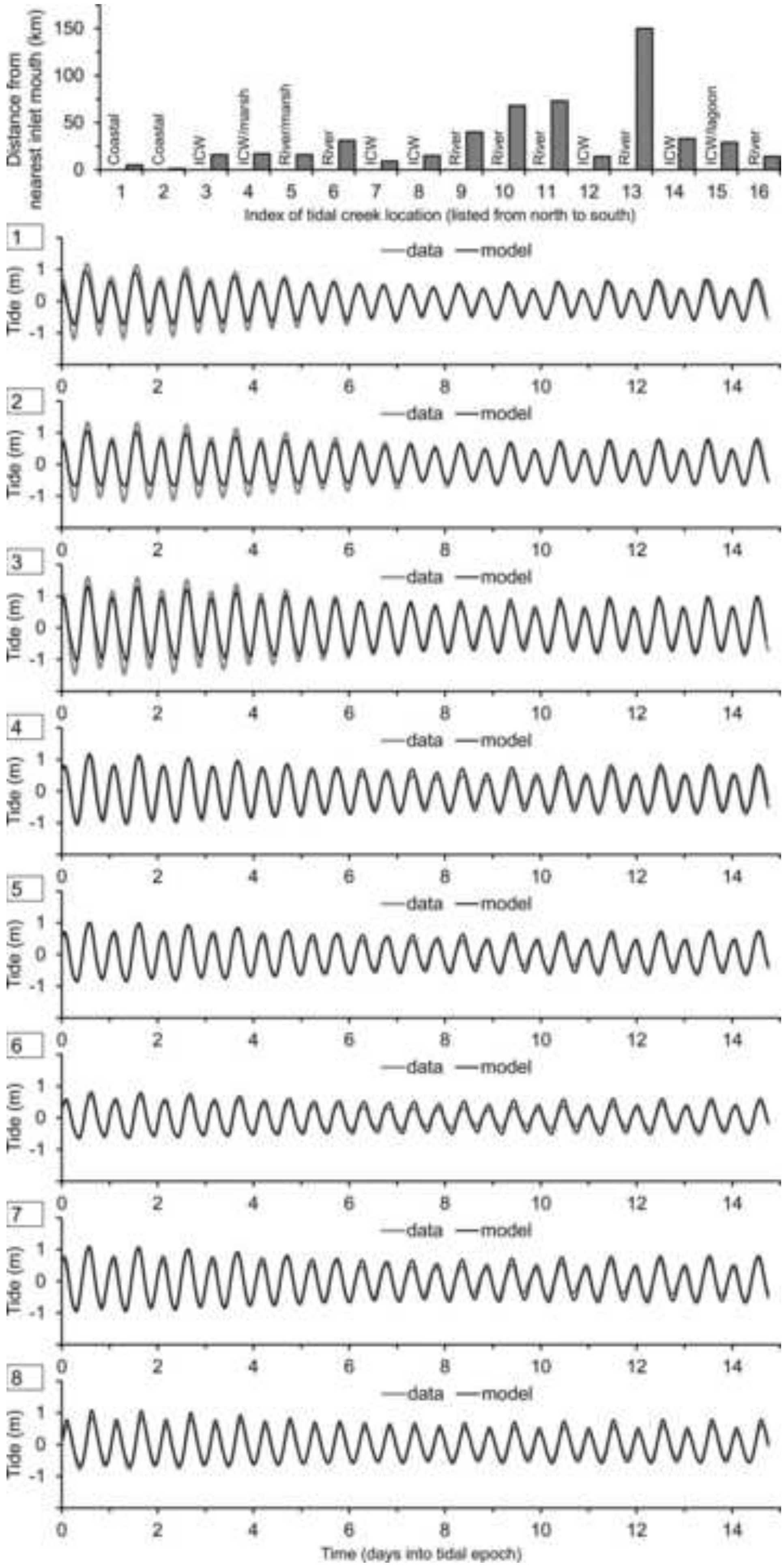

Distance from nearest inlet mouth (km)
150
100
50
0
Coastal
Coastal
ICW
ICW/marsh
River/marsh
River
ICW
ICW
River
River
River
ICW
River
ICW
ICW/lagoon
River
1 2 3 4 5 6 7 8 9 10 11 12 13 14 15 16
Index of tidal creek location (listed from north to south)
1
2
3
4
5
6
7
8
data
model
Tide (m)
1
0
-1
0 2 4 6 8 10 12 14
Time (days into tidal epoch)

**Figure B2 (continued)**

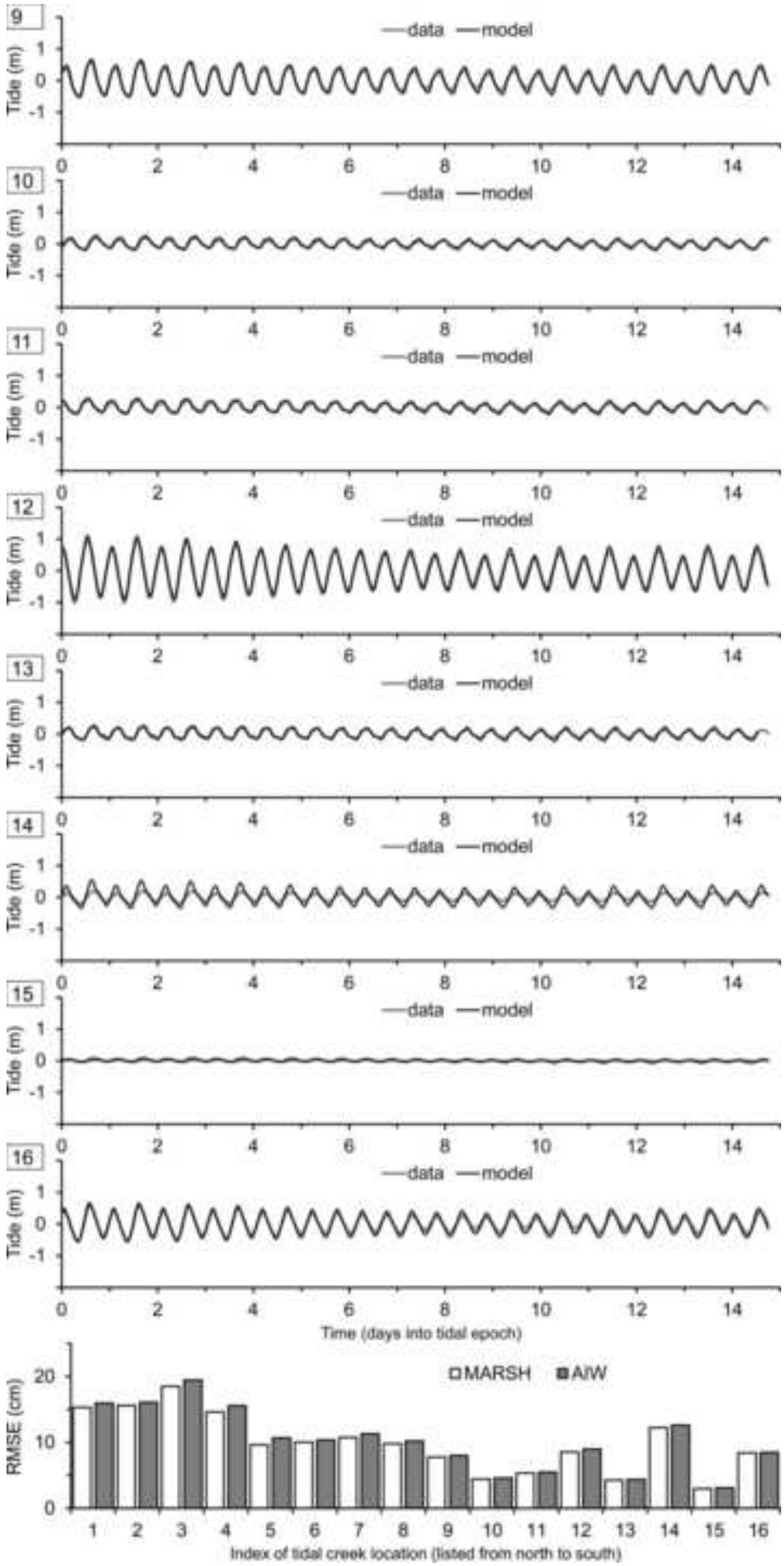

**Figure B3a**

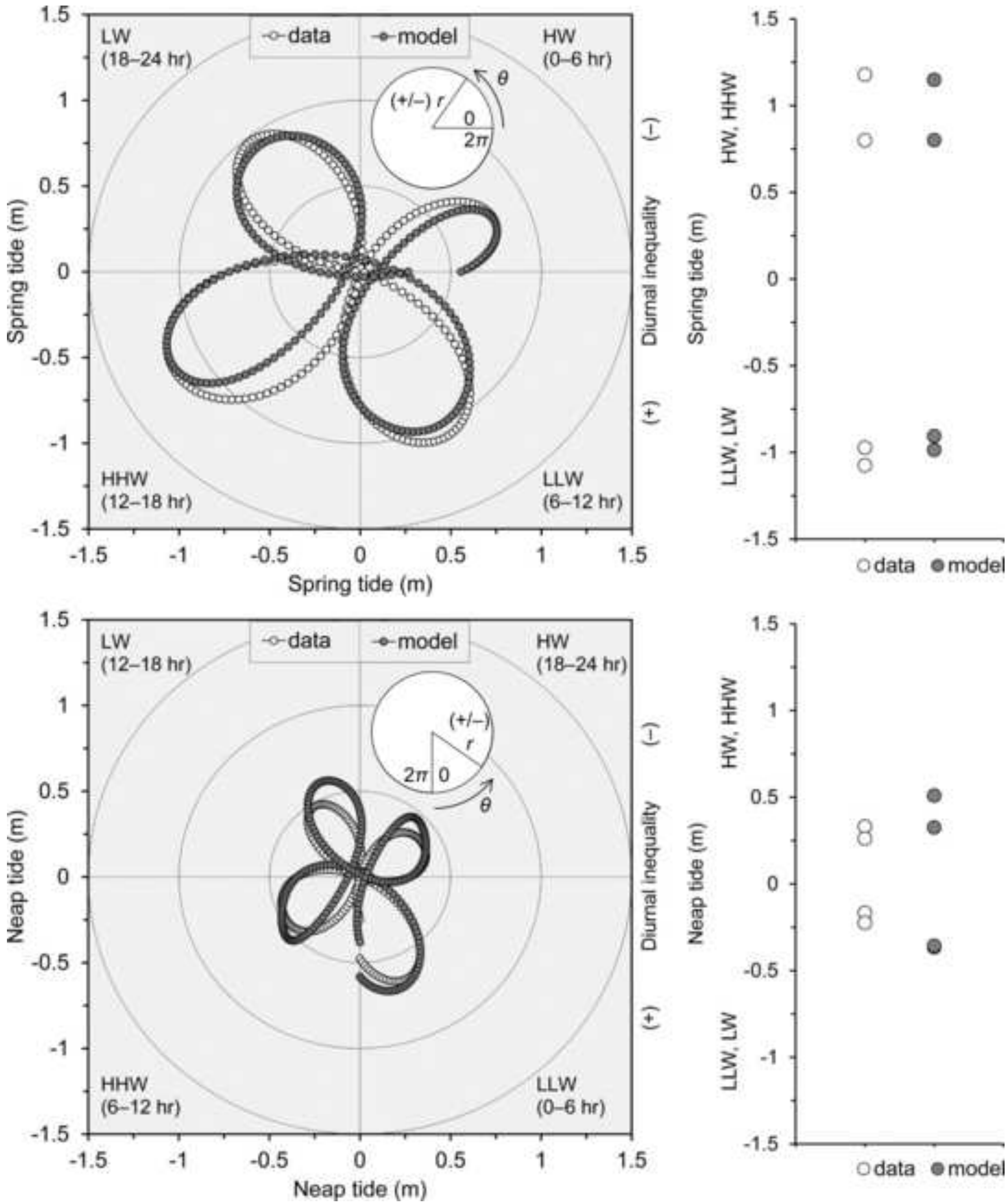

data
model
LW
(18–24 hr)
HW
(0–6 hr)
HHW
(12–18 hr)
LLW
(6–12 hr)
(+/–) r
0
2π
θ
(–)
(+)
Diurnal inequality
Spring tide (m)
HW, HHW
LLW, LW
LW
(12–18 hr)
HW
(18–24 hr)
HHW
(6–12 hr)
LLW
(0–6 hr)
Neap tide (m)

Figure B3b

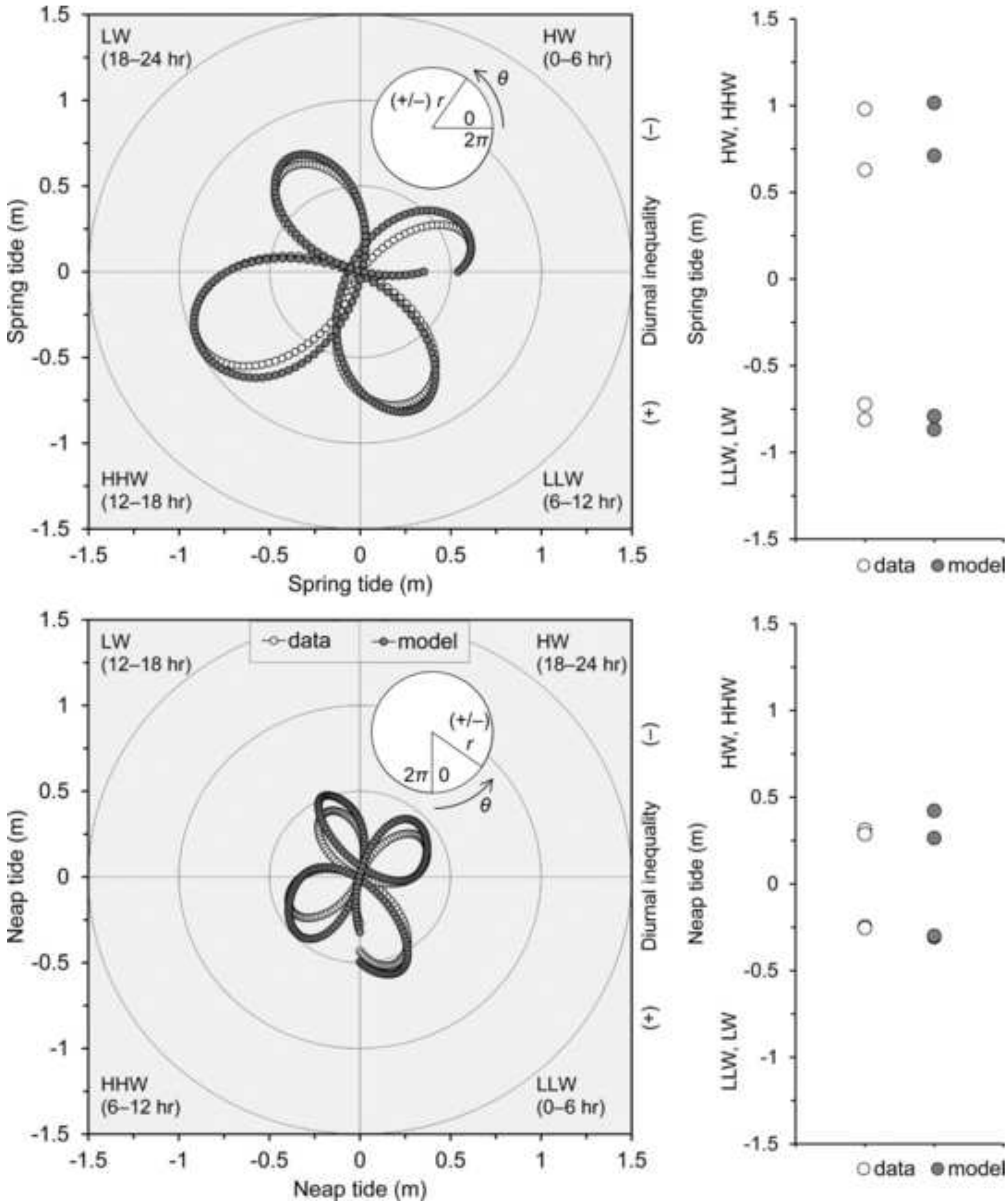
LW
(18–24 hr)
HW
(0–6 hr)
HHW
(12–18 hr)
LLW
(6–12 hr)
(+/–) r
θ
0
2π
Spring tide (m)
Diurnal inequality
(–)
(+)
HW, HHW
LLW, LW
data
model
LW
(12–18 hr)
HW
(18–24 hr)
HHW
(6–12 hr)
LLW
(0–6 hr)
Neap tide (m)

Table 1. There are 64 inlets located along the South Atlantic Bight coastline. The inlets are listed is in the order of north to south. Partition 1 includes the 27 inlets from Winyah Bay, South Carolina to the Florida/Georgia border (grey shaded). Partition 2 includes the 37 inlets for the coastline of the southern portion of North Carolina, the northern portion of South Carolina and Florida’s east coast.

| No. | Inlet | No. | Inlet |
|---|---|---|---|
| 1 | Bogue Inlet, NC | 33 | Wassaw Inlet, GA |
| 2 | Bear Inlet, NC | 34 | Ossabaw Inlet, GA |
| 3 | Browns Inlet, NC | 35 | St. Catherine Inlet, GA |
| 4 | New River Inlet, NC | 36 | Sapelo Inlet, GA |
| 5 | New Topsail Inlet, NC | 37 | Doboy Inlet, GA |
| 6 | Middle Inlet, NC | 38 | Altamaha River Entrance, GA |
| 7 | Wrightsville Inlet, NC | 39 | Little St. Simon Island Pass, GA |
| 8 | Masonboro Inlet, NC | 40 | Sea Island Pass, GA |
| 9 | Myrtle Grove Inlet, NC | 41 | St. Simon Inlet, GA |
| 10 | Southport Entrance, SC | 42 | St. Andrew Inlet, GA |
| 11 | Lockwoods Folly Inlet, SC | 43 | St. Mary’s Inlet, GA/FL |
| 12 | Shallotte Inlet, SC | 44 | Nassau Inlet, FL |
| 13 | Tubbs Inlet, SC | 45 | Fort George Inlet, FL |
| 14 | Little River Inlet, SC | 46 | Mayport Entrance, FL |
| 15 | North Inlet, SC | 47 | St. Augustine Inlet, FL |
| 16 | Winyah Bay Entrance, SC | 48 | Matanzas Inlet, FL |
| 17 | North Santee River Entrance, SC | 49 | Ponce de Leon Inlet, FL |
| 18 | South Santee River Entrance, SC | 50 | Port Canaveral Entrance, FL |
| 19 | Bulls Bay Entrance, SC | 51 | Sebastian Inlet, FL |
| 20 | Bull Island Pass, SC | 52 | Fort Pierce Inlet, FL |
| 21 | Dewees Island Pass, SC | 53 | St. Lucie Inlet, FL |
| 22 | Wild Dunes Pass, SC | 54 | Jupiter Inlet, FL |
| 23 | Charleston Harbor Entrance, SC | 55 | Lake Worth Inlet, FL |
| 24 | Folly Island Pass, SC | 56 | South Lake Worth Inlet, FL |
| 25 | Wadmalaw River Entrance, SC | 57 | Boca Raton Inlet, FL |
| 26 | Edisto Inlet, SC | 58 | Hillsboro Inlet, FL |
| 27 | St. Helena Inlet, SC | 59 | Port Everglades Entrance, FL |
| 28 | Hunting Island Pass, SC | 60 | Bakers Haulover Canal, FL |
| 29 | Old Island Pass, SC | 61 | Government Cut, FL |
| 30 | Port Royal Inlet, SC | 62 | Norris Cut, FL |
| 31 | Tybee Roads Entrance, SC/GA | 63 | Bear Cut, FL |
| 32 | Little Tybee Island Pass, GA | 64 | Biscayne Bay Entrance, FL |

Table 2. Definitions and descriptions of tidal datums (after NOAA Tides and Currents, 2015).

| Acronym | Definition | Description |
|---|---|---|
| HAT | Highest astronomical tide | The elevation of the highest predicted astronomical tide expected to occur at a specific tide station over the National Tidal Datum Epoch |
| MHHW | Mean higher high water | The average of the higher high water height of each tidal day observed over the National Tidal Datum Epoch |
| MHW | Mean high water | The average of all the high water heights observed over the National Tidal Datum Epoch |
| MSL | Mean sea level | The arithmetic mean of hourly heights observed over the National Tidal Datum Epoch |
| MLW | Mean low water | The average of all the low water heights observed over the National Tidal Datum Epoch |
| MLLW | Mean lower low water | The average of the lower low water height of each tidal day observed over the National Tidal Datum Epoch |
| LAT | Lowest astronomical tide | The elevation of the lowest predicted astronomical tide expected to occur at a specific tide station over the National Tidal Datum Epoch |

Table 3. Details of the four meshes used in this study. The size distributions are presented as the average (AVE) plus/minus standard deviation (STD) of the corresponding element edge lengths.

| Mesh | Features | |
|---|---|---|
| COAST | Hard coastline (no inshore features) | |
| | 103,462 nodes | 196,315 elements |
| | 0 inshore nodes (0% of total) | 0 km$^2$ of inshore area |
| | 0 marsh nodes (0% of inshore) | 0 km$^2$ of marsh area |
| | Size distribution (inshore): | 0 AVE ± 0 STD m |
| | Size distribution (marsh): | 0 AVE ± 0 STD m |
| INLET | COAST + inlets (64 total), estuaries, rivers and lagoons | |
| | 272,216 nodes | 481,107 elements |
| | 169,367 inshore nodes (62% of total) | 4010 km$^2$ of inshore area |
| | 0 marsh nodes (0% of inshore) | 0 km$^2$ of marsh area |
| | Size distribution (inshore): | 142 AVE ± 109 STD m |
| | Size distribution (marsh): | 0 AVE ± 0 STD m |
| AIW | INLET + Atlantic Intracoastal Waterway | |
| | 317,487 nodes | 550,424 elements |
| | 214,638 inshore nodes (68% of total) | 4276 km$^2$ of inshore area |
| | 0 marsh nodes (0% of inshore) | 0 km$^2$ of marsh area |
| | Size distribution (inshore): | 127 AVE ± 104 STD m |
| | Size distribution (marsh): | 0 AVE ± 0 STD m |
| MARSH | AIW + marshes | |
| | 540,114 nodes | 1,005,008 elements |
| | 437,282 inshore nodes (86% of total) | 7947 km$^2$ of inshore area |
| | 245,772 marsh nodes (56% of inshore) | 3672 km$^2$ of marsh area |
| | Size distribution (inshore): | 123 AVE ± 89 STD m |
| | Size distribution (marsh): | 119 AVE ± 72 STD m |

Table 4. Tidal ellipse parameters are listed for the four shelf gaging stations (GR, R2, R5 and R6), based on data and model results. SEMA = semi-major axis; ECC = eccentricity; INC = inclination; and PHA = phase. Ratio values are calculated as: $SEMA_{AIW}$ ÷ $SEMA_{COAST}$; and $SEMA_{MARSH}$ ÷ $SEMA_{AIW}$.

| | Data | Model | | | | Ratio (–) | |
|---|---|---|---|---|---|---|---|
| | | COAST | INLET | AIW | MARSH | A:C | M:A |
| GR | | | | | | | |
| SEMA($m\ s^{-1}$) | 0.249 | 0.219 | 0.269 | 0.273 | 0.254 | 1.25 | 0.93 |
| ECC (–) | –0.269 | –0.168 | –0.198 | –0.201 | –0.213 | | |
| INC (°) | 148.5 | 159.1 | 159.8 | 156.7 | 156.0 | | |
| PHA (°) | 285.6 | 272.4 | 280.6 | 281.7 | 285.1 | | |
| R2 | | | | | | | |
| SEMA($m\ s^{-1}$) | 0.312 | 0.274 | 0.318 | 0.321 | 0.303 | 1.17 | 0.94 |
| ECC (–) | –0.337 | –0.301 | –0.296 | –0.296 | –0.309 | | |
| INC (°) | 146.5 | 157.7 | 156.9 | 156.8 | 155.6 | | |
| PHA (°) | 287.0 | 270.6 | 276.4 | 277.3 | 279.8 | | |
| R5 | | | | | | | |
| SEMA($m\ s^{-1}$) | 0.297 | 0.266 | 0.301 | 0.303 | 0.285 | 1.14 | 0.94 |
| ECC (–) | –0.310 | –0.280 | –0.279 | –0.280 | –0.294 | | |
| INC (°) | 144.5 | 156.9 | 156.2 | 156.1 | 155.1 | | |
| PHA (°) | 289.6 | 277.2 | 282.8 | 283.6 | 285.9 | | |
| R6 | | | | | | | |
| SEMA($m\ s^{-1}$) | 0.289 | 0.260 | 0.289 | 0.291 | 0.285 | 1.12 | 0.98 |
| ECC (–) | –0.363 | –0.353 | –0.349 | –0.348 | –0.350 | | |
| INC (°) | 149.2 | 156.7 | 155.7 | 155.7 | 155.4 | | |
| PHA (°) | 278.5 | 266.2 | 271.4 | 272.2 | 273.8 | | |

Table A1. The South Atlantic Bight was split into two partitions based on the denser (estuary) and sparser (estuary) portions of the coastline.

| | 1st partition of SAB | 2nd partition of SAB |
|---|---|---|
| General description | Denser (estuary) coastline | Sparser (estuary) coastline |
| Geography | Florida/Georgia border to Winyah Bay, South Carolina | Florida’s east coast, northern portion of South Carolina and North Carolina |
| Coastline length | 350 km | 950 km |
| Number of inlets | 27 | 37 |
| Average inlet width | 2900 m | 600 m |
| Inlet-inlet coastline | 15 km | 26 km |
| Total inlet flux area | 232,000 $m^2$ | 76,000 $m^2$ |
| Average inlet flux area | 8600 $m^2$ | 2200 $m^2$ |
| Estuaries (shape) | | |
| Number of convergent | 9 | 5 |
| Number of prismatic | 8 | 7 |
| Number of divergent | 0 | 6 |
| Estuaries (type) | | |
| Number of coastal plain | 9 | 5 |
| Number of piedmont | 6 | 5 |
| Number of barrier island | 3 | 11 |
| Marsh area | 3300 $km^2$ | 400 $km^2$ |
| Lagoon area | 0 $km^2$ | 2200 $km^2$ |